Accepted Manuscript

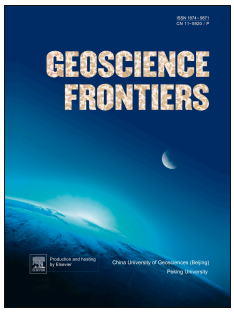

Thermal evolution of an ancient subduction interface revealed by Lu–Hf garnet geochronology, Halilbağı Complex (Anatolia)

Amaury Pourteau, Erik E. Scherer, Simon Schorn, Rebecca Bast, Alexander Schmidt, Lisa Ebert

PII: S1674-9871(18)30079-3

DOI: 10.1016/j.gsf.2018.03.004

Reference: GSF 689

To appear in: *Geoscience Frontiers*

Received Date: 1 November 2017

Revised Date: 13 February 2018

Accepted Date: 8 March 2018

Please cite this article as: Pourteau, A., Scherer, E.E., Schorn, S., Bast, R., Schmidt, A., Ebert, L., Thermal evolution of an ancient subduction interface revealed by Lu–Hf garnet geochronology, Halilbağı Complex (Anatolia), *Geoscience Frontiers* (2018), doi: 10.1016/j.gsf.2018.03.004.

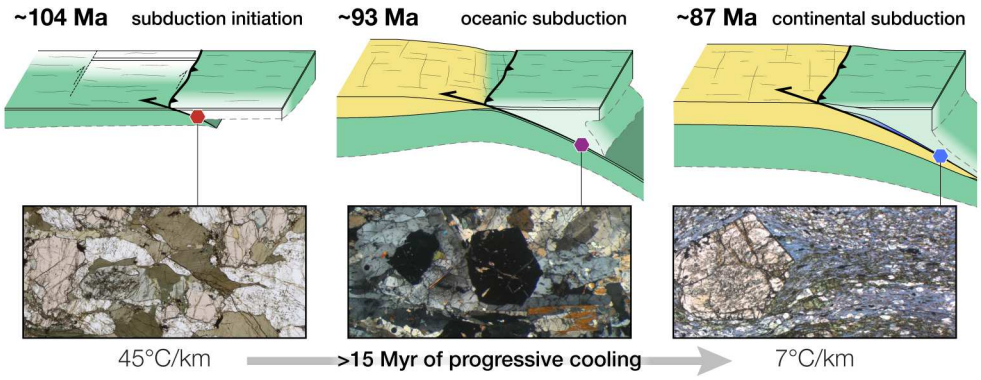

Thermal evolution of an ancient subduction interface revealed by Lu–Hf garnet geochronology, Halilbağı Complex (Anatolia)

Amaury Pourteau[a,d,*], Erik E. Scherer[b], Simon Schorn[c], Rebecca Bast[b,e], Alexander Schmidt[a], Lisa Ebert[a]

[a] *Institut für Erd- und Umweltwissenschaften, Universität Potsdam, Karl-Liebknecht-Straße 24–25, 14476 Potsdam–Golm, Germany*

[b] *Münster Isotope Research Centre, Institut für Mineralogie, Westfälische Wilhelms-Universität Münster, Correnssstraße 24, 48149 Münster, Germany*

[c] *Department of Geological Sciences, University of Cape Town, Private Bag X3, Rondebosch 7701, South Africa*

[d] *Earth Dynamics Research Group, ARC Centre of Excellence for Core to Crust Fluid Systems (CCFS), The Institute for Geoscience Research (TIGeR), School of Earth and Planetary Sciences, Curtin University, GPO Box U1987, WA 6845, Australia*

[e] *Institut für Geologie und Mineralogie, Universität zu Köln, Zülpicher Str. 49b, D-50674 Köln, Germany*

*Corresponding author.

Now address: Earth Dynamics Research Group, ARC Centre of Excellence for Core to Crust Fluid Systems (CCFS), The Institute for Geoscience Research (TIGeR), School of Earth and Planetary Sciences, Curtin University, GPO Box U1987, WA 6845, Australia

E-mail address: amaury.pourteau@curtin.edu.au

Abstract

The thermal structure of subduction zones exerts a major influence on deep-seated mechanical and chemical processes controlling arc magmatism, seismicity, and global element cycles. Accretionary complexes exposed inland may comprise tectonic blocks with contrasting pressure–temperature (P–T) histories, making it possible to investigate the dynamics and thermal evolution of former subduction interfaces. With this aim, we present new Lu–Hf geochronological results for mafic rocks of the Halilbağı Complex (Anatolia) that evolved along different thermal gradients. Samples include a

lawsonite–epidote blueschist, a lawsonite–epidote eclogite, and an epidote eclogite (all with counter-clockwise P–T paths), a prograde lawsonite blueschist with a "hairpin"-type P–T path, and a garnet amphibolite from the overlying sub-ophiolitic metamorphic sole. Equilibrium phase diagrams suggest that the garnet amphibolite formed at ~0.6–0.7 GPa and 800–850 °C, whereas the prograde lawsonite blueschist records burial from 2.1 GPa and 420 °C to 2.6 GPa and 520 °C. Well-defined Lu–Hf isochrons were obtained for the epidote eclogite (92.38 ± 0.22 Ma) and the lawsonite–epidote blueschist (90.19 ± 0.54 Ma), suggesting rapid garnet growth. The lawsonite–epidote eclogite (87.30 ± 0.39 Ma) and the prograde lawsonite blueschist (ca. 86 Ma) are younger, whereas the garnet amphibolite (104.5 ± 3.5 Ma) is older. Our data reveal a consistent trend of progressively decreasing geothermal gradient from granulite-facies conditions at ~104 Ma to the epidote-eclogite facies around 92 Ma, and the lawsonite blueschist–facies between 90 and 86 Ma. Three Lu–Hf garnet dates (between 92 and 87 Ma) weighted toward the growth of post-peak rims (as indicated by Lu distribution in garnet) suggest that the HP/LT rocks were exhumed continuously and not episodically. We infer that HP/LT metamorphic rocks within the Halilbağı Complex were subjected to continuous return flow, with "warm" rocks being exhumed during the tectonic burial of "cold" ones. Our results, combined with regional geological constraints, allow us to speculate that subduction started at a transform fault near a mid-oceanic spreading centre. Following its formation, this ancient subduction interface evolved thermally over more than 15 Myr, most likely as a result of heat dissipation rather than crustal underplating.

Keywords: subduction; Lu/Hf dating of garnet; metamorphic sole; eclogite; blueschist; lawsonite

1. Introduction

The thermal structure of subduction zones has a major influence on deep-seated mechanical and chemical processes controlling arc magmatism, seismicity, and global element cycles (e.g., Poli and Schmidt, 1995; Kirby et al., 1996; Hacker et al., 2003; Bebout, 2007; Peacock, 2009; Spandler and Pirard, 2013; Galvez et al., 2016). Research on modern subduction zones and numerical models have demonstrated that 'cold' subduction zones, such as at the Izu–Bonin trench (W Pacific), are characterised by more intense arc magmatism and a deeper extent (down-dip) of the seismogenic zone as compared to 'warmer' examples, such as the Cascadia subduction zone (NE Pacific; e.g.,

Peacock and Wang, 1999; Kirby, 2000; van Keken et al., 2002). Strongly deflected isotherms indeed result in delayed dehydration of the upper oceanic slab, causing embrittlement of deep portions of the subducted slab and water flux into the deep, hence hot mantle wedge (e.g., Schmidt and Poli, 1998; Hacker et al., 2003; Abers et al., 2013). The thermal structure of many modern subduction zones has been determined by a combination of geophysical measurements and numerical modelling (e.g., Peacock et al., 2005; Syracuse et al., 2010; Wada et al., 2015), and has been shown to generally correlate with the subduction parameters, i.e. the age of incoming lithosphere, the rate of subduction, and the slab dip angle (e.g., van Keken et al., 2011). Rapid change of these parameters is occurring where spreading ridges are subducted (e.g. East Pacific trench–trench-ridge triple junctions), and where oceanic plateaus are accreted (e.g. Ontong–Java Plateau against the Solomon island arc; Yakutat plateau beneath southern Alaska). In addition, young and incipient subduction zones, such as from southernmost New Zealand to the Macquarie Ridge Complex (e.g., Eberhart-Phillips and Reyners, 2001; Meckel et al., 2003) can be expected to have a transient thermal structure if heat from the bottom of the mantle wedge is dissipated slowly into the down-going slab. The thermal evolution of the subduction interface during such transient tectonic stages has only been explored by a few dynamic modelling studies (e.g., Kincaid and Sacks, 1997; Gerya et al., 2002; Mehl et al., 2003; Hall, 2012; Duretz et al., 2016), and the results vary according to the different model settings, boundary conditions, and physical parameters used.

Important constraints on the thermal evolution of subduction interfaces can be obtained from associated high-pressure (HP)/low-temperature (LT) oceanic rocks (typically blueschists and eclogites) exposed at the Earth's surface. Blueschists and eclogites occur along former plate boundaries as coherent tectonic units (e.g., Angiboust et al., 2009; Vitale Brovarone et al., 2013), or chaotic complexes—either 'mélanges' or deep accretionary complexes (e.g., Cloos, 1982; Federico et al., 2007). *Coherent* oceanic HP units are commonly inferred to have detached from the subducting plate and accreted to the bottom of the overriding mantle or crust initially as large tectonic slices (Ruh et al., 2015, and references therein). The underplating of buoyant continental crust during the transition to collision plays a crucial role in the exhumation of coherent HP/LT units (e.g., Agard et al., 2009). In contrast, *chaotic* complexes are commonly regarded as sections of palaeo-subduction channels in which 1–100-metre-scale lenses of HP oceanic rocks (metamorphosed pelagic

sedimentary rocks, basalt, gabbro, and ultramafic rocks) are exhumed during ongoing subduction (Shreve and Cloos, 1986; Gerya et al., 2002; Agard et al., 2009). In any case, protracted subduction accretion along the slab interface may tectonically juxtapose HP/LT metamorphosed oceanic—and ultimately continental—rocks, recording different stages of the evolution of the subduction zone. Deciphering and comparing the metamorphic evolution of individual tectonic lenses of HP oceanic rocks in such complexes might therefore provide first-order information on the internal dynamics and thermal evolution of subduction channels. This approach, however, has only been undertaken by a few petrochronological studies (Anczkiewicz et al., 2004; Krebs et al., 2008; Hyppolito et al., 2016), which all suggested that changes of the thermal gradient down-dip of an ancient slab interface may last several tens of Myr.

In the present study, we address the evolution of a HP metamorphic complex, at Halilbağı in western Central Anatolia (Fig. 1), in which the constituent tectonic blocks evolved along various, commonly counter-clockwise metamorphic P–T paths. Available geochronological constraints suggest that the Halilbağı Complex formed soon after subduction initiation, i.e. in a potentially thermally instable setting. To test the hypothesis of a progressive cooling of the former subduction interface, we selected mafic samples that are representative of the variety of metamorphic histories encountered in the Halilbağı Complex, investigated their petrological evolution, determined the major- and trace-element compositions of whole rocks and metamorphic phases, and dated them with garnet Lu–Hf geochronology. The two end-member samples, a garnet amphibolite and a lawsonite blueschist, were further investigated using equilibrium phase diagram calculations to link the garnet Lu–Hf ages to P–T conditions. Our petrochronological analysis allows us to compare the pressure–temperature–time (P–T–t) evolution of metamorphic rocks having different petrological histories and provides new insights on the tectonic history of this complex and the thermal evolution of juvenile subduction zones in general.

2. Geological setting

The Halilbağı Complex (Fig. 1) is exposed in the western part of the Sivrihisar Massif, in Western Anatolia and comprises tectonic slices of mafic, siliciclastic, ultramafic, and carbonate rocks that were subducted to high-pressure (HP), low-temperature (LT) conditions prior to exhumation. It is part of

the Tavşanlı Zone, a regional mid-Cretaceous blueschist-facies metamorphic belt (Okay, 1986) that formed along the northern margin of a Gondwana-derived micro-continent. The latter collided with the composite south-Eurasian margin during the Palaeocene, following the closure of the Neotethys Ocean (see Pourteau et al., 2016, and references therein). The Halilbağı Complex was intercalated between a non-metamorphosed ophiolitic unit and metamorphosed stratigraphically coherent units (Fig. 1). The ophiolite comprises mainly serpentinised peridotite and subordinate layered gabbro, mafic volcanic- and deep-marine sedimentary rocks, as well as localised amphibolite with rare garnet-bearing domains (Gautier, 1984; Sarıfakıoğlu et al., 2010). The stratigraphically coherent tectonic units consist of interbedded carbonate-, siliciclastic-, and minor mafic rocks (Fig. 1b) with incipient blueschist- to lawsonite–jadeite blueschist- and epidote-blueschist facies metamorphic imprints (Davis and Whitney, 2006; Çetinkaplan et al., 2008; Davis, 2011). In the eastern Sivrihisar Massif, similar units were partly overprinted during a medium-pressure, medium temperature (MP/MT) metamorphic event (Whitney et al., 2010; Seaton et al., 2013). White mica Ar–Ar geochronology yielded 90–82 Ma dates from blueschist-facies assemblages and 64–55 Ma dates for the amphibolite-facies overprint (Seaton et al., 2009; Seaton et al., 2013). The latter overprint is restricted to the eastern part of the Sivrihisar Massif, as elsewhere in the Tavşanlı Zone oceanic accretionary complexes and distal continental units retained pristine lawsonite- and jadeite-bearing assemblages indicating burial *and* exhumation along very low geothermal gradients (<8 °C/km; Okay et al., 1998; Okay, 2002; Plunder et al., 2015).

Northward intra-oceanic subduction below the obducted ophiolite is thought to have started during the early Late Cretaceous, as indicated by Ar–Ar dating of hornblende (generally clustered at 95–90 Ma; see reviews by Çelik et al., 2011; van Hinsbergen et al., 2016) from the sub-ophiolitic LP/HT metamorphic soles exposed across western and southern Anatolia. The age of the metamorphic sole exposed in the Sivrihisar Massif (near Memik; Fig. 1b) is constrained only by an imprecise garnet–whole rock Sm–Nd date of 102 ± 33 Ma (Sarıfakıoğlu et al., 2010). Maastrichtian (72–66 Ma) blueschist-facies metamorphism recently documented in more proximal continental units further south (Candan et al., 2005; Pourteau et al., 2010; Pourteau et al., 2014) indicates that subduction of the continental margin continued until the end of the Cretaceous. Greenschist-facies retrogression in these units took place around 65–60 Ma (Pourteau et al., 2013) and can be linked to the MP/MT

overprint in the eastern Sivrihisar Massif (Whitney et al., 2010). Non-deformed Early Eocene granite and monzonite plutons such as those exposed in the study area (Fig. 1b; Sherlock et al., 1999; Shin et al., 2013) are common in the Tavşanlı Zone. They crosscut tectonic contacts between the ophiolite and the various units of the Tavşanlı Zone (Harris et al., 1994).

The Halilbağı Complex (Fig. 1) comprises up to km-long and hm-thick tectonic lenses of metabasalt, calc-schist, marble, quartzite, manganiferous quartzite, metatuff, (micro)gabbro, and serpentinite (Davis and Whitney, 2006; Çetinkaplan et al., 2008; Whitney et al., 2014). Centimetre- to metre-long pods of eclogite, blueschist, and serpentinite occur among larger lenses of isoclinally-folded marble and quartzite (Davis and Whitney, 2008; Whitney et al., 2014). Different rock-types are generally juxtaposed without intervening matrix, although in the northern domain, dominated by blueschist and eclogite, blocks seem to be embedded in lawsonite blueschist (Davis and Whitney, 2006; Çetinkaplan et al., 2008; Whitney et al., 2014). The western part of the complex is dominated by calc-schist and marble, and was interpreted as a distinct tectonic unit by Gautier (1984) and Çetinkaplan et al. (2008). Davis (2011) proposed different boundaries and relative structural positions on the basis of structural criteria, and distinguished two “belts” made of tectonic slices that can be followed laterally for hundreds of metres. Çetinkaplan et al. (2008), Whitney et al. (2014) and Fornash et al. (2016) described a more fragmented pattern, with metre- to hectometre-long blocks, especially for the blueschist–eclogite domain. Owing to the assemblage of MORB-type metabasalt, Mn quartzite, metagabbro, and serpentinite, there is a general agreement on the oceanic origin of the blueschist–eclogite domain (Çetinkaplan et al., 2008; Davis, 2011; Whitney et al., 2014). The calc-schist– and marble-dominated domain, in contrast, was more likely derived from the leading edge of the subducted continental margin, despite the lack of continental substratum (Çetinkaplan et al., 2008). The structural relationship between the blueschist–eclogite and calc-schist-marble domains has been variously interpreted. Çetinkaplan et al. (2008) regarded the calc-schist–marble unit as a klippe on top of the blueschist–eclogite domain, whereas Davis (2011) depicted it as a window. Our own observations in the field as well as on satellite images do not allow us to discriminate between these two interpretations. Therefore, cross-sections representing both settings are shown in Fig. 1.

The Halilbağı Complex is famous for its lawsonite eclogite (Whitney and Davis, 2006) but it actually includes the complete range from lawsonite blueschist to epidote-bearing eclogite with all

intermediates (e.g., omphacite-bearing blueschist; glaucophane-bearing eclogite) as well as highly retrogressed rocks (chlorite–epidote pods; see Whitney and Davis, 2006; Çetinkaplan et al., 2008; Davis and Whitney, 2008). Available P–T estimates for the metamorphic peak range from 600 °C at 1.6 GPa for epidote eclogite to 450–500 °C at 2.2–2.6 GPa for lawsonite-bearing blueschist and eclogite (Davis and Whitney, 2006; Çetinkaplan et al., 2008; Davis and Whitney, 2008). Davis and Whitney (2006) suggested that the blocks in the Halilbağı Complex shared a common retrograde history from ~40 km depth to the surface (i.e., less than 1.4 GPa). Reconstructed P–T loops for tectonic blocks of the blueschist–eclogite domain are commonly counter-clockwise, with the prograde path being in the epidote stability field and a retrograde lawsonite+epidote blueschist–facies overprint. Rare epidote eclogite contains prograde and retrograde epidote, <9 modal % amphibole, and <1 modal % lawsonite (Davis and Whitney, 2006; this study). However, prograde lawsonite has been documented in the blueschist–eclogite domain (Davis and Whitney, 2006; Çetinkaplan et al., 2008). The mafic lens within the calc-schist-marble unit (Fig. 1c) is composed of epidote-free blueschist and eclogite that contains pristine prograde and peak lawsonite and probably followed a clockwise "hairpin"-type P–T path (Ernst, 1988) with tectonic burial and exhumation along very low T/depth gradients (<7 °C/km; Çetinkaplan et al., 2008). The preservation of lawsonite in the Halilbağı Complex, and the Tavşanlı Zone in general (e.g., Okay et al., 1998; Plunder et al., 2015), indicates progressive cooling during decompression, i.e., exhumation coeval with continuous subduction (see Ernst, 1988).

3. Previous geochronological data

A few geochronological studies have been conducted in the Halilbağı Complex (see review by Fornash et al., 2016). Sherlock and co-workers documented widespread excess ^{40}Ar in HP/LT white mica throughout the entire mid-Cretaceous blueschist-facies belt encompassing the Halilbağı Complex (Sherlock et al., 1999; Sherlock and Arnaud, 1999), and hence used Rb–Sr geochronology on white mica as a more reliable means to date HP metamorphism. For the Halilbağı Complex, these authors published two concordant Rb–Sr ages: 80.1 ± 1.6 Ma (2 SD) for a metachert and 82.8 ± 1.7 Ma from the blueschist-facies retrograde foliation of a metamafic rock. These were interpreted to slightly postdate peak metamorphism (Sherlock et al., 1999). Recently, Mulcahy et al. (2014) presented two Lu–Hf isochron ages (whole rock–lawsonite–garnet) for a lawsonite eclogite (91.1 ± 1.3 Ma) and a

garnet–lawsonite blueschist (83.3 ± 1.8 Ma) from the Halilbağı Unit. The authors did not present detailed petrographic descriptions, phase compositions, or Lu distribution in garnet, so it remains unclear whether the blueschist-facies metamorphism at ca. 83 Ma was prograde or retrograde (i.e. overprinting an eclogite-facies paragenesis). Lastly, Fornash et al. (2016) presented UV-laser in-situ Ar–Ar white-mica analyses for various rock types and mineral assemblages representative for the diversity encountered in the Halilbağı Complex. Mean weighted dates of 93.0 ± 1.8 and 90.2 ± 1.4 Ma (2 SD) for two lawsonite eclogite samples were regarded representative for the age of peak metamorphism (~500–550 °C at up to 2.6 GPa), and one of 81.2 ± 2.2 Ma for an epidote eclogite was interpreted as a cooling age. Interestingly, blueschist and quartzite from their study yielded large intra-sample, inter-grain age scatter (commonly from ~84 to ~109 or even ~126 Ma), which according to the authors might be explained by the preservation of prograde, peak, and retrograde metamorphic stages in low-strain samples. The existing geochronological data does not allow testing whether rocks with different P–T paths evolved synchronously or diachronously. The complete tectonic development of the Halilbağı Complex, from the accretion of oceanic units to the exhumation of HP metamorphic rocks, thus remains in question, and further data are required to unravel its thermal and structural evolution.

4. Material and methods

4.1. Samples

To test the working hypothesis that the array of published P–T paths for the Halilbağı Complex record the early refrigeration of the subduction zone, we selected, out of >40 metamafic rock samples, five representing different metamorphic evolutions. Four mafic blueschist and eclogite samples from the Halilbağı Complex and one HT/LP mafic sample from the metamorphic sole of the overlying ophiolite were investigated.

(i) Garnet amphibolite SIV1301 (39°32’50’’N, 31°32’11’’E) was collected from the sub-ophiolitic metamorphic sole at Memik (Fig. 1b), which is composed of predominant bimineralic amphibolite and hornblendite, and rare garnet-bearing domains (Gautier, 1984; Sarıfakıoğlu et al., 2010).

(ii) Epidote eclogite HAL1255 (39°36'04"N, 31°14'51"E) was collected from the core of a competent block (or 'pod'; Davis and Whitney, 2008) that is enveloped by a retrogressive schistose rind of phengite, chlorite, aegirine–augite, titanite, epidote, and sodic-calcic amphibole.

(iii) Lawsonite–epidote blueschist HAL1243 (39°35'37"N, 31°16'16"E) stems from a locality studied in detail by Davis and Whitney (2008), Mulcahy et al. (2014; 91.1 ± 1.3 Ma Lu–Hf date), and Fornash et al. (2016). This sample was collected from a block of garnet-bearing blueschist enveloped by a schistose rind of coarse-grained actinolite, epidote, lawsonite, phengite, and titanite.

(iv) Lawsonite–epidote interlayered blueschist and eclogite HAL1241 was collected in the vicinity of HAL1243 (Fig. 1c) and exhibits mm-thick alternation of glaucophane-rich and glaucophane-poor layers.

(v) Lawsonite blueschist HAL1304 (39°35'27"N, 31°14'05"E) is a foliated lawsonite-, garnet- and clinopyroxene-bearing blueschist and stems from a lens comprising foliated mafic blueschist and isolated eclogitic pods in the calc-schist–marble unit (Fig. 1c). Some compositional layering is marked by variable modes of sodic pyroxene.

4.2. Analytical methods

4.2.1. Sample preparation

The mineral separation procedure consisted of crushing fist-size rock pieces down to cm-size fragments using a hammer. Part of the crushed sample was powdered in an agate shatterbox for whole-rock analysis. The rest was processed twice through a disk mill using first a 2-mm and then a 1-mm spacing between the disks. Intact garnet crystals were handpicked after each pass. Impure handpicked garnet grains coarser than 1 mm were processed separately through a second round of crushing and handpicking to obtain a purer fraction. The remaining amount of crushed samples was then rinsed with water, dried with acetone, and split into grain size fractions by sieving. Fractions below 1 mm were processed through a Frantz® magnetic separator to isolate garnet from clinopyroxene and amphibole, and other minerals with lower magnetic susceptibility (e.g., lawsonite, epidote, white mica). To avoid fractionating garnet cores from rims on the basis of their Fe contents,

the magnet current and side tilt were adjusted such that all garnet was collected within a single fraction. From this, intact idiomorphic garnet crystals and crystal fragments were handpicked under a binocular microscope. From the intermediate magnetic fractions, polycrystalline aggregates of low-Lu/Hf groundmass phases (hereafter "matrix") were handpicked. Particular care was taken to select fragments devoid of garnet and, when possible, lawsonite, which may have high Lu/Hf (Tribuzio et al., 1996; Mulcahy et al., 2009). Matrix separates consisted predominantly of hornblende for SIV1301, omphacite for HAL1255 and HAL1241, and blue amphibole for HAL1243 and HAL1304, but also contained minor phases (e.g., epidote, rutile, titanite, phengite, ilmenite). Because these matrix samples were handpicked from specific magnetic fractions, they are not exactly equivalent to the whole rock minus garnet (and lawsonite) porphyroblasts. Nevertheless, they are useful for constraining the low–Lu/Hf end of isochrons and, when compared to bomb-digested whole rocks, detecting inherited zircon in the latter.

To investigate the major- and trace element compositions of the dated garnets, intact idiomorphic garnet crystals were mounted in epoxy and polished down to their approximate geometric centres. As garnet commonly concentrates Lu in its innermost core, which might be easily missed during the preparation process (e.g., Skora et al., 2006), several grains of similar size were mounted together. Mounted garnet grains were then analysed by electron microprobe, and crystals with the highest contents in MnO for a specific sample were considered to expose near-core portions and were investigated *in-situ* by LA-ICP-MS. The textural context of garnet and other phases was studied using polished thin-sections.

4.2.2. Major- and trace element analysis

Bulk-rock powders were analysed for their major-element compositions using X-ray fluorescence (XRF) and for iron oxidation state using potassium-dichromate titration at the GeoForschungsZentrum Potsdam (Germany). Only relevant data are cited in the text but the complete results for bulk rocks can be found in Appendix A. Mineral major-element analysis was performed on a JEOL8200 electron probe microanalyser (EPMA) at the University of Potsdam using natural and synthetic minerals as standards. Amphibole structural formulae were calculated using the spreadsheet of Locock (2014). Ferrous-, and ferric iron contents of garnet and pyroxene were calculated following Droop (1987). All

289 iron in epidote was assumed as ferric. Representative mineral analyses are given in Appendix B. Trace
290 element contents were determined using a CETAC LSX-213 laser ablation system coupled with a
291 Thermo Scientific Element 2 single-collector ICPMS at the University of Potsdam. The spot size was 25
292 or 50 µm for the 'HAL' samples, and 100 µm for SIV1301 because of low trace-element concentrations
293 in the latter. A laser repetition rate of 10 Hz was used. The fused-glass reference material BIR1-G
294 (GeoReM preferred values of Jochum et al., 2005) was used for external standardisation with ^{44}Ca as
295 an internal standard. In-situ trace element analyses of garnet porphyroblasts are given in Appendix C.
296
297 *4.2.3. Lu–Hf geochronology*
298 The Lu–Hf geochronology was performed at the Münster Isotope Research Centre, Westfälische
299 Wilhelms-Universität, Germany, following the procedure described by Smit et al. (2010), which is
300 briefly summarized here. Mineral separates (garnet, hornblende, matrix) were weighed into Savillex®
301 Teflon® vials, washed for 10 minutes in 1.0–1.5 M HCl at room temperature, and then rinsed with
302 Milli-Q H_2O. Mineral separates and whole-rock powders were then spiked with a mixed ^{176}Lu–^{180}Hf
303 tracer. Mineral separates were digested sequentially in concentrated HF–HNO_3 (2:1) and 10 M HCl on
304 a hotplate at 120 °C, drying the sample down between steps. This process was repeated until the
305 addition of the HCl resulted in a clear solution, indicating full digestion of the target phase. This
306 selective digestion procedure dissolves the target phases whereas some refractory minerals that
307 potentially contain inherited Hf components (e.g., rutile and zircon) are left behind (Lagos et al., 2007).
308 Unfortunately, titanite inclusions *are* dissolved by this procedure, potentially offsetting garnet
309 fractions to lower $^{176}Lu/^{177}Hf$ and $^{176}Hf/^{177}Hf$ values. Although the $^{176}Lu/^{177}Hf$ of titanite varies widely
310 (e.g., 0.008 to 0.5, on the basis of El Korh et al. (2009) data), it is lower than that of the garnet in any
311 sample measured here. If titanite crystallized essentially at the same time as garnet (or equilibrated
312 with it), then digestion of titanite inclusions with the garnet would merely shift the latter down the
313 isochron without affecting its Lu–Hf age. If, however, titanite formed substantially before the garnet
314 and variable Lu/Hf among garnet fractions reflects differing amounts of titanite inclusions present, an
315 inverse relationship between Lu/Hf and apparent age would be expected. No such relationship is
316 observed in our data. We conclude that either titanite formed approximately contemporaneously
317 with garnet (or that garnet isotopically equilibrated with early titanite). Alternatively, the relatively

low Hf concentration in titanite (≤11 ppm; El Korh et al., 2009) as compared to zircon (~10,000 ppm Hf; Scherer et al., 2000), would mean that any age difference between titanite inclusions and host garnet would have a much smaller effect on the measured garnet date than digested zircon inclusions would have.

Whole-rock powders were digested in closed Savillex® vials with concentrated HF–HNO_3 (2:1) on a hotplate at 120 °C and were then evaporated to dryness. Vials were then refilled with HF–HNO_3 (2:1), closed and placed along with a few mL H_2O into steel-jacketed Teflon® autoclaves at 180 °C for 5 days to ensure complete digestion. The digested samples were dried down, taken up in 6 M HCl, and diluted to 3 M HCl–0.1 M ascorbic acid (HAsc). The chemical separation of Lu and Hf was performed on heat-shrunk Teflon® columns containing Eichrom® Ln-Spec resin following the procedure of Sprung et al. (2010), which is based on that of (Münker et al., 2001), but with additional purification steps for Hf and Lu. Our method differed from that of Sprung et al. (2010) in that we loaded the sample with HAsc on the *first* stage Ln-spec column rather than on the second stage because we did not require an HAsc-free matrix cut for subsequent Sm–Nd analysis. In addition, we employed a third stage (column I of Bast et al., 2015) to ensure complete Lu removal from the Hf cuts. The ion-exchange chromatography procedure is detailed in Appendix D. Isotope ratio measurements of Hf and Lu were performed on a Thermo® Neptune Plus MC-ICP-MS at the Institute of Mineralogy, University of Münster, Germany following the procedure of Bast et al. (2015).

4.2.4. Estimation of the metamorphic P–T evolutions

The metamorphic P–T evolution of samples SIV1301 and HAL1304 was investigated by calculating equilibrium phase diagrams ('pseudosections') and mineral composition isopleths using THERMOCALC v.3.45 (Powell and Holland, 1988) and an updated version of the Holland and Powell (2011) thermodynamic dataset (file tc-ds62.txt, created 06/02/2012) with the activity–composition models of White et al. (2014) and Green et al. (2016). Quartz, albite, rutile, titanite, lawsonite, and aqueous fluid are assumed to have pure end-member compositions. Modelled phase abbreviations are as follows: augite (aug), diopside (dio), omphacite (o), biotite (bi), garnet (g), actinolite (act), glaucophane (gl), hornblende (hb), muscovite (mu), paragonite (pa), albite (ab), plagioclase (pl),

chlorite (chl), epidote (ep), lawsonite (law), orthopyroxene (opx), quartz (q), rutile (ru), titanite (sph), ilmenite (ilm), tonalitic melt (L) and aqueous fluid (H_2O).

For garnet amphibolite SIV1301, we employed the HT 'augite' model as it allows partitioning of Al in the tetrahedral site (Green et al., 2016). The bulk-rock XRF analysis was simplified by disregarding minor amounts of Cr_2O_3 and by subtracting apatite for P_2O_5. Furthermore, MnO was disregarded as component for sample SIV1301 as it is found only in minor concentrations, even in garnet cores (Fig. 3f; Appendix B). This simplified Na_2O–CaO–K_2O–FeO–MgO–Al_2O_3–SiO_2–H_2O–TiO_2–O_2 (NCKFMASHTO) model composition (Table 1), with the titration-determined Fe oxidation state, was used for our calculations and H_2O was considered to be in excess. The robustness of this latter assumption was tested by calculating an isobaric T–M(H_2O) phase diagram, where M(H_2O) represents the molar H_2O content of the system.

For lawsonite blueschist HAL1304, we used the subsolidus 'diopside' model for HAL1304 as it includes the clinopyroxene solvi (diopside–omphacite–jadeite; Green et al., 2016). As for SIV1301, Cr_2O_3 and P_2O_5 were disregarded, but MnO must be considered as a component in order to model the formation of the spessartine-rich garnet core (Sps_{40}; Fig. 3e,j). Unfortunately, Mn is not yet included in the activity-composition models for amphibole and clinopyroxene. Nonetheless, these phases are major constituents of the investigated sample, despite their low MnO-contents (Appendix B). To account for the MnO sequestered in amphibole and clinopyroxene, we arbitrarily reduced the MnO content to 90% of the measured whole-rock value. We acknowledge that this procedure is qualitative at best as the 'effective' MnO available for garnet growth (i.e. not sequestered by amphibole and clinopyroxene, which are so far modelled in the MnO-free system) is largely unknown. The conditions of garnet nucleation should therefore be interpreted with care. This MnNCKFMASHTO model system composition, together with a lowered $Fe^{3+}/\sum Fe$ (permitting improved convergence between model and observations), was used to model the formation of the Mn-rich garnet core. Strong compositional zoning of garnet in HAL1304 (see below) precludes that the bulk-rock composition reflects the effective bulk composition at metamorphic peak. To account for chemical fractionation during prograde garnet growth, the effective bulk composition at peak conditions was recalculated in the Mn-free NCKFMASHTO model system by subtracting the average composition of garnet (estimated on the basis of the profile shown in Fig. 3j and assuming spherical porphyroblasts) for all MnO. For

HAL1304, H_2O was considered to be in excess, which is supported by the presence of pristine lawsonite and glaucophane (see Clarke et al., 2006).

5. Results

5.1. Petrography and major-element mineral compositions

5.1.1. Garnet amphibolite (SIV1301)

This sample contains plagioclase, amphibole, garnet, clinopyroxene, and ilmenite (Fig. 2a). Garnet, highly variable in mode (0–20 vol.%), forms subhedral to anhedral porphyroblasts ranging from a few micrometres (inclusion free) to ~3 cm in diameter (poikilitic). Poikilitic grains contain rounded inclusions of plagioclase, amphibole, and clinopyroxene. Garnet composition is uniform ($Alm_{54–55}Prp_{22–23}Sps_{2–3}Grs_{20}$; Fe# = $Fe^{2+}/(Fe^{2+}+Mg)$ = 0.70–0.71), except for some slight diffusion-induced zoning at the rim ($Alm_{56}Prp_{18}Sps_3Grs_{23}$; Fe# = 0.76), which follows the grain boundaries whether they are resorption surfaces or preserved crystal faces (Fig. 3a,f). Garnet is in textural equilibrium with clinopyroxene ($En_{35–40}Fs_{14–17}Wo_{47–48}$; Fe# = 0.28–0.31), plagioclase ($An_{90–95}Ab_{5–10}$), and some (relatively Fe^{3+}-poor) amphibole, although the replacement of garnet as well as clinopyroxene by amphibole is a common feature (Fig. 2a). The amphibole is magnesio-(ferri-)hornblende and has widely variable Si- (6.3–7.1 atoms per formula unit, 'a.p.f.u.') and Fe^{3+} contents ($X_{Fe^{3+}} = Fe^{3+}/[Al+Fe^{3+}]$ = 0.29–0.74). Amphibole (Amp_1) in textural equilibrium with garnet and plagioclase is coarse grained and clusters at Si = 6.6–6.7 a.p.f.u, and Ti = 0.15–0.18 a.p.f.u. Titanium in amphibole generally decreases with increasing Si content. Finer-grained, Fe^{3+}-richer, Ti-poorer amphibole formed at a later stage, along amphibole grain boundaries. Plagioclase and clinopyroxene generally exhibit deformation twinning. Plagioclase cores contain clusters of minute inclusions of idiomorphic amphibole and garnet, and thick inclusion-free rims. No compositional difference between plagioclase core and rims was noticed. Thin symplectite, generally comprising magnesio-hornblende, anorthite ($An_{93–94}$), and albite ($Ab_{91–95}$), developed at contacts between amphibole and other phases.

In the garnet amphibolite SIV1301, the assemblage Grt–Cpx–Amp_1–Pl_1–Ilm is inferred to have been stable at peak conditions (Fig. 4). It was overprinted by thin Amp_2–Pl_2–Ab symplectite possibly caused by 'reversal reaction' between the peak phases and a crystallising, voluminously subordinate silicate melt phase (Kriegsman, 2001; Brown, 2002). Supra-solidus peak metamorphism

would be somehow consistent with the high Ti-contents of Amp_1, and is tested below in light of equilibrium phase diagram calculations. By contrast with other Anatolian localities of sub-ophiolitic amphibolite (Önen and Hall, 1993; Dilek and Whitney, 1997; Plunder et al., 2016), the metamorphic sole at Memik displays no blueschist-facies overprint.

5.1.2. Epidote eclogite (HAL1255)

This sample is composed of euhedral to subhedral porphyroblasts of garnet (up to 2 mm in diameter) in a matrix of omphacite, epidote, rutile (rimmed by titanite), phengite, and accessory quartz and zircon (Fig. 2b). Veinlets of un-oriented chlorite and white mica cut across the sample. Garnet is concentrically zoned with two main successive, conformable growth phases (Fig. 3b). The prograde Grt_1 core ($Alm_{54–61}Prp_{7–18}Sps_{2–13}Grs_{21–28}$) shows an outward decrease in Fe# and Mn content. A very thin Grt_2 rim on Grt_1 accounts for a small increase of Mn, Ca, and Fe# ($Alm_{50–52}Prp_{15}Sps_{4–5}Grs_{28–31}$; Fe# = 0.77–0.79; Fig. 3g). Inclusions in garnet are quartz, epidote, rutile, and zircon. Matrix omphacite ($Jd_{13–44}Aeg_{2–23}$; Fe# = 0.18–0.32) displays complex compositional zoning (Appendix E), which generally makes its textural relationship with garnet difficult to determine. Nevertheless, omphacite in clear textural equilibrium with garnet (Omp_2: $Jd_{19–31}Aeg_{2–13}$, Fe# = 0.26–0.31) occasionally has a more jadeitic core (Omp_1: $Jd_{31–41}Aeg_{4–23}$). Two texturally-late Fe^{3+}-richer groups ($Jd_{23–28}Aeg_{17–23;}$ and $Jd_{13–23}Aeg_{6–17}$, respectively) might have formed along with or after Grt_2. Matrix epidote occurs as small (~0.15 mm) anhedral grains that display either pulsed, core-to-rim increase of $X_{Fe^{3+}}$ or irregular zoning resulting from several resorption events within $X_{Fe^{3+}}$ = 0.18–0.29. Titanite is absent in garnet but ubiquitous in the matrix, where it commonly rims rutile. Rare white mica in the eclogitic paragenesis is highly substituted phengite (Si = 3.29–3.48 a.p.f.u. and Fe# = 0.27–0.38). No amphibole was found in this sample.

In contrast to the other samples, HAL1255 and its retrogressive rind contain no lawsonite, pseudomorphs after lawsonite, or glaucophane. The entire metamorphic history of this epidote eclogite was thus likely confined to the stability field of epidote.

5.1.3. Lawsonite–epidote blueschist (HAL1243)

The main mineral assemblage in HAL1243 (Fig. 2c) consists of garnet, glaucophane, actinolite, lawsonite, omphacite, epidote, rutile (rimmed by titanite), phengite, chlorite, and accessory zircon. Subhedral to euhedral garnet porphyroblasts tend to concentrate along layers. Garnet displays concentric zoning (Fig. 3c) with three distinct growth stages. The prograde Grt_1 core ($Alm_{48–53}Prp_{8–17}Sps_{5–15}Grs_{25–30}$) shows a general rimward decrease in Fe# (from 0.86 to 0.76; Fig. 3h). Within Grt_1, a slight but sharp Ca and Mn increase marks the transition from Grt_{1a} to Grt_{1b} across which Fe# decreases steadily. Both Grt_{1a} and Grt_{1b} are in turn partially resorbed and overgrown by a rim of Grt_2 ($Alm_{54–56}Prp_{7–8}Sps_{11–12}Grs_{25–2}$; Fe# = 0.88–0.89). Inclusions in garnet are epidote ($X_{Fe^{3+}}$ = 0.15–0.18), quartz, glaucophane ($X_{Fe^{3+}}$ = 0.08, Fe# = 0.38), phengite (Si = 3.50 a.p.f.u.), chlorite (Fe# = 0.26), euhedral titanite near the core and rutile in outer part of Grt_1. Rutile is also present in Grt_2, occasionally rimmed by titanite. In the matrix, glaucophane has Gln_1 cores ($X_{Fe^{3+}}$ < 0.07; Fe# = 0.27–0.30) overgrown by Gln_2 rims ($X_{Fe^{3+}}$ = 0.11–0.21; Fe# = 0.29–0.32). Actinolite (Na_B = 0.22–0.47; Fe# = 0.18–0.23; $X_{Fe^{3+}}$ = 0.10–0.58) is observed in textural equilibrium with Gln_2. Matrix epidote is anhedral and shows mainly bimodal compositional zoning: Ep_1 ($X_{Fe^{3+}}$ = 0.10–0.19) overgrown by Ep_2 ($X_{Fe^{3+}}$ = 0.25–0.27). Lawsonite forms euhedral porphyroblasts up-to-1-mm long, and aggregates up-to-2-mm across. Lawsonite crystals are generally aligned with the weak matrix foliation. Inclusions in lawsonite have the following compositions: glaucophane Gln_2 (occasionally with Gln_1 cores), omphacite Omp_2 ($Jd_{20}Aeg_{20}$), and epidote Ep_2. Clinopyroxene, which occurs as isolated euhedral to subhedral grains, defines a compositional trend from omphacite $Jd_{37}Aeg_{13}$ to aegirine–augite $Jd_{16}Aeg_{22}$. Because of complex zoning, chronological relationships are generally difficult to determine. However, the highest jadeite contents are found in anhedral inclusions in the outer part of Grt_1. Comparison with the progressive Fe^{3+} enrichment of amphibole and epidote suggests a progressive increase in aegirine and decrease in jadeite. Sharp grain boundaries indicate textural equilibrium between lawsonite and garnet rims. Inclusions in lawsonite are predominantly actinolite and subordinate glaucophane Gln_2 (occasionally with Gln_1 cores), omphacite Omp_2 ($Jd_{20}Aeg_{20}$), and epidote Ep_2. White mica is highly substituted phengite (Si = 3.48–3.52 a.p.f.u.; Fe# = 0.32–0.35). Less-substituted phengite (Si = 3.42 a.p.f.u.) is locally intergrown with unzoned chlorite (Fe# = 0.32–0.33). Rutile in the matrix, in contrast to rutile in Grt_1, is rimmed by titanite.

Textural relationships suggest that the assemblage Grt_1–Omp–Gln_1–Ep_1–Qz–Ttn-(later Rt)±Chl formed during prograde- to peak metamorphic stages, and was overprinted by the assemblage Grt_2–Gln_2–Act–Lws–Ep_2–Ph–Ttn (Fig. 4). This sequence points to a counter-clockwise P–T path with entry into the lawsonite stability field during the retrograde evolution.

5.1.4. Lawsonite–epidote interlayered blueschist and eclogite (HAL1241)

This sample displays alternating blueschist (omphacite-poor), and eclogitic (glaucophane-poor) domains and comprises garnet, lawsonite, omphacite, glaucophane, actinolite, epidote, rutile (rimmed by titanite), phengite, quartz, and chlorite (Fig. 2d). Garnet porphyroblasts (up to 3 mm in diameter) exhibit similar features in the blueschist and eclogite domains, with a prograde Grt_1 interior ($Alm_{56–60}Prp_{8–22}Sps_{2–7}Grs_{23–28}$; Fe# = 0.77–0.88) and a rimward decrease in Mn content and Fe# (Fig. 3d). The Grt_1 domains are slightly resorbed and overgrown by a Grt_2 rim ($Alm_{61–65}Prp_{7–8}Sps_{2–6}Grs_{26–30}$), which marks a sharp increase in Fe# (0.89–0.90) and Mn and Ca contents (Fig. 3i). Garnet contains inclusions of epidote ($X_{Fe^{3+}}$ = 0.19–0.21), quartz, omphacite ($Jd_{26–27}Aeg_{19–21}$ and Fe# = 0.18–0.19; $Jd_{37–41}Aeg_{5–13}$ and Fe# = 0.33–0.39), titanite (in garnet cores), rutile (in garnet rims), phengite (too small for analysis), and accessory apatite and zircon. Lawsonite and chlorite were also observed in the innermost core of one garnet crystal (Fig. 2e,f). In the matrix, omphacite (Omp_1 cores, $Jd_{38–48}Aeg_{2–16}$; Omp_2 rims, $Jd_{23–30}Aeg_{9–37}$) and epidote (Ep_1 cores: $X_{Fe^{3+}}$ = 0.16–0.19; Ep_2 rims: $X_{Fe^{3+}}$ = 0.24–0.26) are bimodally zoned. Amphibole has glaucophane cores (Fe# = 0.35–0.39; $X_{Fe^{3+}}$ =0.00–0.04) overgrown by winchite–actinolite (Act) rims (Na_B = 0.41–0.52; Fe# = 0.25–0.26; $X_{Fe^{3+}}$ =0.27–0.54). Lawsonite, forming coarse xenomorphic porphyroblasts up to 2 mm across, contains inclusions of glaucophane, actinolite, two generations each of omphacite and epidote, and titanite with occasional rutile in its core. White mica Ph_2 associated with Grt_2, Omp_2, and Act has an Si content of 3.49–3.51 a.p.f.u. and an Fe# of 0.36–0.42. Rutile in the matrix, in contrast to rutile inclusions in garnet, is rimmed by titanite.

Three successive metamorphic stages are thus identified in HAL1241: a possible early prograde assemblage containing Lws_1–Ep_1–Chl–Ph_1, the prograde- to peak paragenesis Grt_1–Omp_1–Gln–Ep_1–Ph_1–Qz–Rt, and the retrogressive paragenesis Grt_2–Omp_2–Act–Ep_2–Lws_2–Ph_2–Ttn (Fig. 4). As

for HAL1243, the lawsonite blueschist-facies overprint points to exhumation along a lower thermal gradient than during burial. Nevertheless, the early growth of lawsonite (observed in a single garnet grain) suggests initial burial through the stability field of lawsonite.

5.1.5. Lawsonite blueschist (HAL1304)

The dominant assemblage of HAL1304 consists of glaucophane, lawsonite, clinopyroxene, garnet, and rutile (Fig. 2g). Garnet ($Alm_{31–65}Prp_{3–10}Sps_{2–40}Grs_{23–28}$) forms idiomorphic porphyroblasts (up to 3 mm in diameter) that comprise a single growth stage characterised by rimward decreases in Mn and Fe# from 0.93 to 0.87 (Fig. 3e,j). Garnet hosts pristine, commonly idiomorphic lawsonite (up to 200 µm across; Fig. 2h), sodic pyroxene ($Jd_{10–30}Aeg_{18–28}$; i.e., omphacite and aegirine–augite compositions), titanite (in cores), rutile (in rims), apatite in variable amounts, and rare glaucophane (Fe# = 0.38–0.43; $X_{Fe^{3+}}$ = 0.10–0.16). Lawsonite inclusions (within garnet) themselves host glaucophane (too small for analysis), omphacite ($Jd_{26–28}Aeg_{17–22}$), quartz, and trace calcium carbonate. The matrix is generally fine-grained and consists of 50–100 µm grains of sodic clinopyroxene, glaucophane, and lawsonite. Coarse-grained domains in HAL1304 comprise lawsonite crystals up to 500-µm in length and sodic pyroxene aggregates up to 1-mm across, elongated parallel to the foliation. Sodic pyroxene in the matrix (individual grains and up-to-1-mm-thick aggregates) is omphacite ($Jd_{23–33}Aeg_{10–16}$) and displays a core-to-rim increase in jadeite content and Fe# (0.13–0.36). Rare inclusions of phengite in sodic pyroxene (Si = 3.52–3.55 a.p.f.u.; Fe# = 0.33–0.35) and chlorite (Fe# = 0.35) are observed. Matrix glaucophane is slightly zoned with Fe# values (0.28–0.35) and $X_{Fe^{3+}}$ (0.07–0.25) that decrease from core to rim. Thus, in contrast to the other samples, sodic pyroxene and glaucophane display a progressive *decrease* in Fe^{3+} from core to rim. Lawsonite, which is typically idiomorphic, commonly features a core rich in inclusions of glaucophane (Fe# = 0.32–0.35; $X_{Fe^{3+}}$ = 0.05–0.10), titanite, omphacite ($Jd_{26–29}Aeg_{13–22}$), and quartz, and a clearer rim. Iron zoning in lawsonite grains exhibiting an inclusion-rich core and an inclusion-free rim, as reported by Çetinkaplan et al. (2008), was not observed in this sample. Importantly, no epidote and only minor retrograde quartz were observed.

Petrographic observations thus indicate that sample HAL1304 records prograde HP/LT metamorphism within the stability field of lawsonite (Fig. 4), with no hint of a retrograde overprint as

garnet seems to have remained in equilibrium with the matrix over its entire growth interval. Lawsonite remained stable during exhumation, suggesting a "hairpin-type" P–T path (Ernst, 1988).

5.2. Lutetium distribution in garnet

The geological meaning of Lu–Hf dates largely depends on the volumetric distribution of Lu within garnet. Garnet is a major sink for Lu, as illustrated by the typically elevated concentrations in garnet cores (e.g., Lapen et al., 2003; Skora et al., 2006). However, the contribution of the Lu-rich garnet core to the bulk-garnet Lu budget can be minor in comparison to Lu-poorer, but volumetrically more substantial, outer 'shells' (Kohn, 2009; Baxter et al., 2017). Garnet resorption, observed in some of our samples, may cause some Lu redistribution and further skew Lu–Hf dates towards the time of garnet rim growth or re-equilibration (Kelly et al., 2011).

In garnet amphibolite SIV1301, garnet and the other phases are REE poor (<10 ppm total REE). The distribution of Lu in garnet cannot be precisely determined but seems to show a slight inward enrichment (from 0.2 to 0.4 ppm; Appendix C). In epidote eclogite HAL1255, garnet has the highest Lu content (>13 ppm) in its core, a minor peak (~5 ppm) in the mantle, and another peak (~6 ppm) at the rim, corresponding to the Grt_2 overgrowth (Fig. 5). Plotting fraction of the porphyroblast Lu in 10% volume shells reveals that the outer 50 vol.% of the porphyroblast contains 63% of the Lu budget. Lawsonite–epidote blueschist HAL1243 garnet displays a sharp central Lu peak (~35 ppm) and some highs (17–21 ppm) in the core region, and decreases in the outer parts of Grt_1 (<2 ppm). However, the increasing Lu content towards the rim (up to ~20 ppm) has a strong effect on the overall Lu distribution, such that the outer 50 vol.% of the garnet porphyroblast contains 72% of its Lu (Fig. 5). Garnet in lawsonite–epidote interlayered blueschist and eclogite HAL1241 is characterised by a sharp central Lu peak, a high in the garnet mantle, and a further increase towards the Grt_2 rim. As a consequence, 64% of Lu resides in the outer 50 vol.% (Fig. 5). Lawsonite blueschist sample HAL1304 yields a (half-) bell-shaped Lu profile with a broad central peak (up to 66 ppm) grading outwards into a Lu-depleted mantle and rim (<2 ppm). This Lu zoning pattern mimics the smooth zoning in Mn. A minor Lu high (~5 ppm) towards the rim correlates with the transition from titanite- to rutile inclusions (Fig. 5). Unlike the other garnet samples described so far, the Lu distribution is skewed strongly towards the core, with 87% of the Lu in the inner 50 vol.% of garnet.

545

546 **5.3. Lu–Hf geochronology results**

547 All concentrations and isotope ratios are given in Table 2. Regressions were calculated using the
548 model-1 fit of Isoplot/Ex (Ludwig, 2012, version 4.15) and a ^{176}Lu decay constant of 1.867×10^{-11} yr^{-1}
549 (Scherer et al., 2001; Söderlund et al., 2004). Uncertainties on dates are quoted as 95% confidence
550 intervals. For all samples, garnet, matrix-phase separates, and autoclaved whole-rock powder
551 (hereafter 'wr') cover a large range in ^{176}Lu/^{177}Hf (Fig. 6).

552 Garnet amphibolite SIV1301 is REE- and Hf poor, presumably because its protolith was a
553 cumulate gabbroic rock. Despite the increased amounts of sample digested (700 mg of wr and up to
554 240 mg of garnet), some fractions yielded imprecise analyses owing to overspiking and low sample-to-
555 blank ratios for Hf (e.g., 17–74; Table 2). The wr and the hornblende fractions do not lie on the same
556 regression line, with hornblende having much lower ^{176}Lu/^{177}Hf and ^{176}Hf/^{177}Hf than the wr (Fig. 6a).
557 Contrasting dates are obtained when pairing garnet with the whole rock instead of the hornblende. A
558 regression of the wr and all three garnet fractions yields a date of 104.6 ± 3.5 Ma (MSWD = 39), and
559 two-point wr–garnet isochrons range between 103.47 ± 0.38 and 105.62 ± 0.37 Ma. The hornblende–
560 garnet regression gives 109.5 ± 1.5 Ma (4 points, MSWD = 7.6) and two-point isochron dates are
561 between 108.78 ± 0.36 Ma and 109.78 ± 0.36 Ma.

562 Epidote eclogite HAL1255 yields a well-constrained matrix–garnet Lu–Hf date of 92.38 ± 0.22
563 Ma (5 points, MSWD = 1.4; Fig. 6b). The autoclaved wr contains substantially more Hf than hotplate
564 digested mineral separates (4.65 vs. 0.13–0.28 ppm, respectively; Table 2). This reflects that zircon
565 and rutile, the two main Hf-rich phases, were fully digested in the autoclaved wr aliquot but not
566 during the selective hotplate digestion procedure used for mineral separates. The wr plots slightly
567 below the matrix–garnet isochron, suggesting that zircon (observed by EPMA) has a partly inherited
568 (pre-metamorphic) Lu–Hf isotopic signature. Part of the offset of the wr could potentially be due to
569 late-grown veinlets of chlorite and phengite, which could not be completely avoided during
570 preparation of the whole-rock powder. Nevertheless, chlorite and phengite are Lu- and Hf-poor
571 phases (Spandler et al., 2003; Spandler and Pirard, 2013), so their contribution to the wr analysis is
572 most likely negligible.

For lawsonite–epidote blueschist HAL1243, the matrix–garnet regression yields 90.19 ± 0.54 Ma (5 points, MSWD = 4.5; Fig. 6c). The high MSWD stems from the highest-$^{176}Lu/^{177}Hf$ garnet aliquot (Grt-b) being offset slightly above the regression line. The other three aliquots yield a well-constrained matrix–garnet isochron at 90.03 ± 0.18 Ma (MSWD = 0.49). For HAL1243, the wr Hf content is again significantly higher than that of the mineral separates (3.08 vs. 0.11–0.19 ppm, respectively) and the wr lies slightly below the matrix–garnet regression. Again, we attribute these features to an inherited Hf component hosted by zircon (observed by EPMA) in the whole rock.

The lawsonite–epidote interlayered blueschist–eclogite HAL1241 gives a matrix–garnet date of 87.30 ± 0.39 Ma (4 points, MSWD = 2.1; Fig. 6d). The garnet aliquot with the highest $^{176}Lu/^{177}Hf$ ratio (Grt-c) lies distinctly above this isochron and was therefore not included in the calculation. The autoclaved wr aliquot is significantly richer in Hf than the mineral separates (2.90 vs. 0.12–0.17 ppm, respectively) and plots far below any matrix–garnet isochron. The Lu–Hf isotopic signature of zircon is therefore predominantly inherited.

For lawsonite blueschist HAL1304, the garnet analyses have consistent $^{176}Lu/^{177}Hf$ (13.8–15.0) and Lu contents (3.22–3.81 ppm; Table 2) but do not lie on a single isochron: A garnet-only regression yields an MSWD of 19. Thus, the matrix–garnet date of 86.9 ± 3.3 Ma (4 points, MSWD = 55) is only loosely constrained (Fig. 6e). Even when excluding the main outlier Grt-d (89.00 ± 0.49 Ma, relative to the matrix), the matrix–garnet regression (86.3 ± 2.9 Ma) has a high MSWD value of 4.1. The autoclaved aliquot wr is again significantly richer in Hf than the mineral separates (1.87 vs. 0.03–0.06 ppm, respectively), but is not displaced from the matrix–garnet trend, suggesting that zircon is present in the wr, but not inherited.

5.4. P–T evolutions

5.4.1. Garnet amphibolite SIV1301

The P–T pseudosection calculated for sample SIV1301 (Fig. 7a) is characterised by large, high-variance assemblage fields and illustrates that the observed assemblage garnet–amphibole–clinopyroxene–plagioclase–ilmenite is stable over a large P–T space on both sides of the H_2O-saturated solidus. The absence of quartz and orthopyroxene narrows down this field to supra-solidus temperatures >830 °C, and above the orthopyroxene-in reaction (Fig. 7a). A small volume of melt (~4 vol.%) related to the

breakdown of hornblende + quartz is predicted to be stable with the observed peak assemblage. The T–M(H_2O) phase diagram calculated at 0.6 GPa (Fig. 7b) shows that the stability of the observed, quartz- and orthopyroxene-absent phase assemblage is restricted to high H_2O contents, always above the solidus. This feature supports our assumption of a fluid-saturated supra-solidus evolution, so that the prediction of a silicate melt phase co-genetic with the peak mineral assemblage cannot be ascribed to mistakenly high H_2O contents. We infer that the amphibolite (Amp_2)–plagioclase (Pl_2)–albite symplectites observed in SIV1301 (Fig. 2a) are the result of 'reaction reversal' (Kriegsman, 2001), i.e. reaction of the crystallising melt with the peritectic phases. This phenomenon has been argued to take place during nearly-isobaric cooling following low degree of partial melting (see Brown, 2002).

The observed compositions of garnet (Grs_{21}; Fe# = 61), plagioclase ($An_{90–95}$ observed vs. An_{92} predicted) and clinopyroxene (Fe# = 28–31), which arguably were part of the peak assemblage, are nearly reproduced in the stability field of the observed phase assemblage (see isopleths on Fig. 7). Uncertainties on the solid-solution models (especially for amphibole) might be invoked but, owing to the flat compositional profile of garnet (Fig. 3f) and the rather uniform composition of clinopyroxene, we infer that these two phases were homogenised through intra-crystalline and intergranular diffusion at near-peak conditions. Clinopyroxene being less homogenised than garnet is consistent with slower Fe–Mg diffusion in the former than in the latter (see e.g., Müller et al., 2013). Using the combined semi-quantitative calibrations of Ernst and Liu (1998), $Al_2O_3^{-}$ and TiO_2 contents of amphibole (11–12 wt.%, and 1.4–1.8 wt.%, respectively) indicate temperatures and pressures up to around 800 °C and 0.5 GPa. Overall, the assemblage is stable over a wide P–T range and is therefore unlikely to yield tight constraints. It is however consistent with formation along an elevated thermal gradient (~45 °C/km).

5.4.2. Lawsonite blueschist HAL1304

The equilibrium phase diagram calculated for sample HAL1304 allows investigating the P–T conditions prevailing for the growth of Mn-rich garnet core in equilibrium with lawsonite, glaucophane and titanite. When the measured iron redox ratio ($Fe^{3+}/\sum Fe = 0.54$) is used for the calculation, garnet core compositions broadly fall in the stability field of rutile, whereas these cores typically host titanite

inclusions (Fig. 3e). The P–T phase diagram obtained for bulk-rock $Fe^{3+}/\sum Fe$ = 0.4 exhibits fields with both garnet and titanite (Fig. 8a), but lower $Fe^{3+}/\sum Fe$ values stabilise diopside with garnet and titanite, which is not observed in this sample and is regarded an artefact of the clinopyroxene solid solution model. The observed garnet core composition ($Sps_{40}Grs_{28}$) is nearly reproduced in the stability field with glaucophane, lawsonite, titanite, chlorite, and quartz and indicates ~420 °C and ~2.1 GPa for the formation of the garnet core (Fig. 8a). The phase diagram calculated for the matrix NCKFMASHTO composition and $Fe^{3+}/\sum Fe$ = 0.4 (Fig. 8b) displays a garnet stability field restricted to higher temperature and pressure as compared to Fig. 8a because of the subtraction of MnO for this calculation. The observed garnet rim composition (Grs_{24}—recalculated using an Sps projection; Fe# = 0.87) is predicted to coexist with the observed phases glaucophane, omphacite, lawsonite, and rutile at ~520 °C and 2.7 GPa.

6. Discussion

6.1. Geological significance of the Lu–Hf dates

Hafnium-rich phases that preserve inherited Hf isotopic compositions—especially zircon, which commonly buffers the Hf budget of a rock—may dramatically impact the Lu–Hf systematics if they are digested along with the target phases (Scherer et al., 2000; Lagos et al., 2007). If these minerals have the same age as garnet, then the bulk-garnet analysis will be shifted down the isochron relative to the composition of pure garnet. This results in shorter isochrons and decreased dating precision, but does not affect the age (Scherer et al., 2000; Baxter and Scherer, 2013; Baxter et al., 2017). If, on the other hand, zircon inclusions are older (inherited), then garnet-controlled mineral isochrons may yield ages that are too young in addition to being less precise (Scherer et al., 2000). The low-pressure, hotplate digestion that we used here for mineral separates avoids such problems by leaving zircon and rutile intact. In contrast, the wr fractions, including any zircon and rutile, were completely digested with high-pressure autoclave digestions. The presence of significant inherited or younger zircon in the wr can therefore be detected, e.g., if the wr plots off an isochron among other minerals that were initially in isotopic equilibrium. In such cases, the wr should be excluded from isochrons: When the zircon is significantly older than the garnet, the garnet-wr and garnet-matrix-wr isochrons will yield

659 spuriously old Lu–Hf dates (e.g., Fig. 5a of Scherer et al., 2000), with the latter also exhibiting
660 excessive scatter.

661 For garnet amphibolite SIV1301, the autoclaved wr fraction has a lower Hf concentration
662 than hornblende and plots *above* the hornblende–garnet regression line. This, as well as the very low
663 bulk-rock Zr (Appendix A) and Hf (Table 2) contents, indicates that there is little or no zircon in this
664 rock. In SIV1301, garnet contains a significantly larger fraction of the whole-rock Hf than the HP/LT
665 samples (Hf_{Grt}/Hf_{wr} = 0.26 vs. 0.02–0.06, respectively), further suggesting that SIV1301 is essentially
666 zircon-free. Consistent with this, no zircon could be found in the thin sections prepared from this rock.
667 We therefore infer that the wr aliquot is not affected by an inherited, zircon-hosted Hf component.
668 The hornblende lies below the garnet-wr tie line. It is not clear why this is the case, but because
669 hornblende formed predominantly after garnet (see Fig. 4), we chose to reference the Lu–Hf garnet
670 dates to the (apparently zircon-free) whole rock instead. The resulting 104.5 ± 3.5 Ma date (Fig. 6a) is
671 inferred to reflect peak metamorphism in SIV1301.

672 Autoclaved wr aliquots of all the HP/LT samples yield Hf contents at least an order of
673 magnitude greater than those of the mineral separates (Table 2), indicating that the hotplate
674 digestion of the latter excluded most, if not all, of the zircon from the analysis. Nevertheless, garnet
675 fractions from all samples except epidote eclogite HAL1255 show resolvable scatter on isochron
676 diagrams. Some of this may result from variable proportions of core and rim material in the bulk
677 garnet aliquots if the growth interval exceeded the typical age uncertainty on two-point matrix–
678 garnet isochrons (e.g., Dragovic et al., 2012; Schmidt et al., 2015). In addition, scatter can also be
679 caused by variable timing of nucleation within the garnet population of a single sample (e.g., Skora et
680 al., 2009). The well-defined multi-point isochron obtained for HAL1255 (92.38 ± 0.22 Ma) suggests
681 that the garnet aliquots had similar proportions of core and rim material and/or that garnet growth
682 was so rapid that the two distinct generations (Fig. 3b) have the same age within analytical resolution.
683 This would be consistent with ~1 Myr prograde garnet growth intervals for HP/LT metamorphic rocks
684 (Dragovic et al., 2012). For lawsonite–epidote blueschist HAL1241, an isochron (MSWD = 2.1) is
685 obtained if outlier Grt-c is excluded, suggesting that the high-$^{176}Hf/^{177}Hf$ of the latter is anomalous.
686 The Lu contents of Grt-c and two out of the three other aliquots are similar. We therefore assume
687 that the Hf concentration of Grt-c was biased by incomplete spike–sample equilibration and consider

688 the matrix–three garnet isochron date of 87.30 ± 0.39 Ma as the best estimate of the average garnet
689 age in HAL1241.

690 Sample HAL1304 does not yield a well-defined Lu-Hf isochron. Because the Lu in HAL1304
691 garnet mostly resides in its cores (Fig. 5), any garnet aliquot containing an unusually high proportion
692 of core material would be enriched in Lu. However, the measured Lu concentrations (3.22–3.91 ppm;
693 Table 2) are similar to the bulk porphyroblast Lu content of HAL1304 garnet (3.47 ppm), calculated
694 using the LA-ICPMS data (Fig. 5; Appendix C). We therefore infer that HAL1304 Grt-d was probably
695 affected by incomplete spike–sample equilibration for Hf and that most of the garnet in HAL1304
696 grew at ~86 Ma.
697
698 **6.2. Comparison of metamorphic evolutions**
699 The investigated metamafic rocks were selected for geochronology on the basis of their contrasting
700 petrological evolutions (see Fig. 4), which were deciphered by petrographic observations and phase
701 compositions (Figs. 2 and 3).
702
703 *6.2.1. Garnet amphibolite SIV1301*
704 Garnet amphibolite SIV1301 evolved along an elevated thermal gradient (~45 °C/km), typical of sub-
705 ophiolitic metamorphic soles. The equilibrium phase diagram together with garnet and clinopyroxene
706 isopleths calculated for SIV1301 (Fig. 7a) suggest peak metamorphism around 800–850 °C and ~0.6–
707 0.7 GPa. Discrepancy between observations and model predictions in terms of garnet and
708 clinopyroxene compositions can be argued to result from nearly complete chemical re-equilibration of
709 those two phases after their growth at HT. Cation diffusion would thus modify the mineral
710 compositions, preventing precise comparison to the calculated isopleths (Fig. 7a). The inferred P–T
711 conditions are compatible with results of empirical geothermobarometric calibrations using systems
712 with low diffusivity such as Al and Ti in amphibole (see section 5.4.1.). We envisage that significant
713 lattice and grain-boundary diffusion of major divalent cations in garnet, and possibly diopside, was
714 favoured by the protracted (>10-Myr-long) cooling of the metamorphic soles of Western Anatolia (see
715 discussion below). Conversely, similar rocks from the metamorphic soles of the Semail ophiolite
716 (Oman), for which much quicker cooling has been demonstrated (Hacker et al., 1996), comprise

717 garnet with well-preserved growth zoning (Soret et al., 2017). High cooling rate might therefore have
718 inhibited mineral re-homogenisation in these rocks, so that mineral assemblage and phase
719 compositions could be well reproduced by Soret et al. (2017). Note that we used the same modelling
720 approach (including identical solid-solution models) as in their study. We therefore consider 0.6–0.7
721 GPa and 800–850 °C as the best P–T estimate for the SIV1301 metamorphic peak.

722 The absence of a blueschist-facies overprint on the upper-amphibolite-facies mineral
723 assemblage is in contrast with the other metamorphic-sole localities in the Tavşanlı Zone and Afyon
724 Zone (Önen, 2003; Plunder et al., 2016) where, hornblende, plagioclase, and clinopyroxene were
725 partly overgrown by glaucophane, lawsonite and occasionally jadeite. Garnet amphibolite SIV1301
726 therefore appears to record isobaric to syn-decompression cooling similar to other metamorphic soles
727 exposed below the far-obducted Tauride ophiolites (see Plunder et al., 2016).

728

729 *6.2.2. Blueschist and eclogite samples*

730 The rimward decrease of #Fe and, to a lesser extent, Ca content in Grt_1 of samples HAL1255,
731 HAL1243, and HAL1241 (Fig. 3) is characteristic for garnet grown during prograde HP/LT
732 metamorphism. Prograde garnet Grt_1 was partly resorbed and overgrown by Grt_2, which appears to
733 have been in equilibrium with the matrix assemblage (Figs. 2 and 3). The slight- (in HAL1255) to
734 pronounced (in HAL1243 and HAL1241) enrichment in Mn (Fig. 3) and Lu (Fig. 5) across the Grt_1–Grt_2
735 boundary is inferred to result from the breakdown and re-growth of garnet, the preferential Mn and
736 HREE host amongst the observed mineral assemblages. In these three samples, the record of garnet
737 grown at the metamorphic peak therefore was lost, in contrast to HAL1304 garnet, which has
738 preserved intact rims of prograde Grt_1. Combined with major element zoning patterns (Fig. 3), the
739 volumetric distribution of Lu in garnet (Fig. 5) indicates that the bulk-porphyroblast garnet Lu–Hf
740 dates (Fig. 6) for HAL1255 (92.4 Ma), HAL1243 (90.2 Ma), and HAL1241 (87.3 Ma) represent weighted
741 averages between the dates of peak Grt_1- and retrograde Grt_2 growth, respectively, whereas the bulk-
742 garnet date for HAL1304 (~86 Ma) marks the start of prograde garnet growth around 420 °C and 2.1
743 GPa (Fig. 8a).

744 The investigated blueschist and eclogite samples were selected on the basis of their relative
745 timing of epidote- and lawsonite formation, regarded as diagnostic of contrasting P–T evolutions. In

746 the absence of reliable quantitative P–T estimates for garnet growth, it admittedly remains uncertain
747 to what extent the contrasting petrological evolutions reflect different P–T evolutions rather than
748 variations of the bulk-rock composition, oxidation state, fluid composition and availability, or open-
749 system behaviour. Amongst our samples, we note that the formation of blueschist vs. eclogite (i.e. the
750 relative abundance of glaucophane and omphacite) might reflect different bulk-rock compositions.
751 For instance, epidote eclogite HAL1255 has lower $Al_2O_3/(CaO+Na_2O+K_2O)$ ($X_{Al_2O_3}$) and higher
752 $CaO/(CaO+FeO_{total}+MnO+MgO+Na_2O$ (X_{CaO}) than the glaucophane-bearing samples (Appendix A),
753 which according to Tian and Wei (2014) would favour the formation of omphacite over glaucophane.
754 These ratios however do not influence the stability of lawsonite vs. epidote at given P and T.
755 Thermodynamic calculations have suggested that epidote stability expands towards higher pressures
756 with increasing bulk-rock Fe^{3+} content (Diener and Powell, 2012). However, large variations in Fe^{3+}
757 content between samples are required to account for the observed differences (Fig. 4), whereas Fe^{3+}
758 contents of epidote, glaucophane, and clinopyroxene in our blueschist and eclogite samples are
759 broadly similar. Eventually, the availability of water during metamorphism might have favoured the
760 formation of epidote over lawsonite in some samples (Clarke et al., 2006). It might thus be envisaged
761 that the absence of lawsonite as well as amphibole in epidote eclogite HAL1255 reflects “dryer”
762 retrogression in this sample as compared to the blueschists. In summary, we cannot completely rule
763 out that differences in the effective bulk composition, especially the amount of free water present
764 during metamorphism, are responsible for the observed petrological differences. Nevertheless, we
765 emphasise that the trend of garnet Lu–Hf dates we obtained does support the working hypothesis of
766 a progressively decreasing geothermal gradient along the former subduction interface. Prograde- and
767 peak mineral assemblages and garnet compositions as observed in lawsonite blueschist HAL1304
768 were reproduced at 2.1 GPa, 410 °C and 2.6 GPa, 530 °C, respectively (Fig. 8). At these conditions, and
769 despite the high iron oxidation state of this rock ($Fe^{3+}/\sum Fe$ = 0.4), the rock evolved far from the
770 stability field of epidote. It therefore seems reasonable to consider that HAL1304 was buried along a
771 distinctly lower thermal gradient than HAL1255, HAL1243, and HAL1241.
772
773 **6.3. Tectonic implications**

774 *6.3.1. Subduction initiation*

775 Sub-ophiolitic LP/HT metamorphic soles, such as at Memik (Fig. 1b), are commonly interpreted to
776 form during the initial stages of subduction, or 'intra-oceanic thrusting' (e.g., Woodcock and
777 Robertson, 1977; Boudier et al., 1988; Hacker, 1990). The two metamorphic-sole localities of the
778 Tavşanlı Zone previously yielded a garnet–amphibole Sm–Nd regression date of 102 ± 33 Ma (Memik;
779 Sarıfakıoğlu et al., 2010), and hornblende Ar–Ar isochron date of 101.1 ± 3.8 Ma (Orhaneli, 200 km
780 further west; Harris et al., 1994), respectively. These dates are within error of our 104.5 ± 3.5 Ma Lu–
781 Hf date for the garnet amphibolite SIV1301. Despite their uncertainties, the Lu–Hf dates stand out of
782 the 95–90-Ma cluster (mainly Ar–Ar in hornblende) obtained from the ophiolite emplaced further
783 south, on the Afyon Zone and on top of non-metamorphosed continental units (Önen, 2003; Daşçı et
784 al., 2015, and references therein). The temperatures reached during sub-ophiolitic metamorphism
785 (650 to 850 °C; see van Hinsbergen et al., 2015; Agard et al., 2016; Plunder et al., 2016; this study)
786 typically exceed Ar closure in hornblende (~530 ± 50 °C; Harrison, 1982). Therefore, we regard the
787 published Ar–Ar hornblende dates as record of the metamorphic-sole cooling, whereas Lu–Hf in
788 garnet approximately dates near-peak conditions. This is corroborated by similar (105–100 Ma) garnet
789 Lu–Hf dates and 99–95 Ma zircon dates that were recently obtained for a metamorphic sole emplaced
790 on top of the non-metamorphosed continental units in southern Central Anatolia (Pınarbaşı ophiolite;
791 Peters et al., 2017).

792 Our estimates of the peak P–T conditions in the Sivrihisar metamorphic sole (Fig. 7) point to
793 a thermal gradient of ~1400 °C/GPa, or ~45 °C/km. According to recent numerical modelling (Grose
794 and Afonso, 2013) and disregarding heat production due to shear heating along the nascent
795 subduction plane, this ratio is equivalent to the geothermal gradient of <15-Myr-old oceanic
796 lithosphere. Subduction initiation therefore likely took place in the vicinity of an active mid-oceanic
797 spreading centre, especially since oceanic spreading in the western Neotethys is largely accepted to
798 have been slow (e.g., Nicolas et al., 1999; Dilek et al., 1999; Stampfli and Borel, 2002; Müller et al.,
799 2008).

800 Subduction initiation around 104 Ma reconciles the initiation of intra-oceanic subduction
801 with the kinematic switch, during the Albian (112–100 Ma), of the African Plate's motion relative to
802 Eurasia from a tangential trajectory to sub-orthogonal convergence (Dewey et al., 1989; Rosenbaum

et al., 2002). Plate reorganisation in the western Tethys realm might thus have triggered the simultaneous inception of several intra-oceanic subduction zones from western Anatolia to Oman (e.g., Boudier and Nicolas, 1985).

The available temporal constraints on the Mesozoic tectonic events in Anatolia allow us to speculate about the locus of subduction initiation. Subduction initiation near oceanic spreading centres might take place at the spreading centre itself (Spray, 1983), along oceanic detachments (Maffione et al., 2015), and along transform faults (Stern and Bloomer, 1992). The former two candidates imply that the new trench forms parallel to the pre-existing spreading centre and that, over the ~15–20 Myr-long history of oceanic subduction, the age of the incoming oceanic slab increased as the continental margin (of the Anatolide–Tauride Block) approached the trench. The ocean floor at the continental margin can be inferred to be Late Triassic in age (230–210 Ma; Sengör and Yilmaz, 1981; Göncüoglu et al., 2010; Speranza et al., 2012), i.e., ~106–126 Myr-old when subduction started (~104 Ma; this study) and ~124–144 Myr-old when it reached the trench (around 86 Ma). Considering the *overall* ~20 mm/yr of Africa–Eurasia convergence during the Late Cretaceous (Rosenbaum et al., 2002), no more than 360 km of oceanic lithosphere can have been consumed along this subduction zone between ~104 and ~86 Ma. Assuming that, at 104 Ma, subduction initiated where the oceanic crust was 15 Myr old (i.e. formed at 119 Ma), extremely slow mid-oceanic half-spreading (~3–4 mm/yr) would be required to generate 360 km of oceanic lithosphere between 230–210 and 119 Ma. Even lower rates should be envisaged given that, during the Late Cretaceous, two to three coeval subduction zones were likely active coevally along the Anatolian segment of the Neotethys Ocean (see Aygül et al., 2016; Çetinkaplan et al., 2016; Pourteau et al., 2016; van Hinsbergen et al., 2016). Such oceanic spreading, as required if the subduction zone was orthogonal to the mid-oceanic ridge, is an order of magnitude slower than assumed for the Neotethys (Müller et al., 2008). We therefore favour a scenario where intra-oceanic subduction was initiated along a transform fault in the vicinity of a mid-oceanic spreading centre, as depicted in Fig. 9. This view seems to reconcile slow regional convergence and coeval consumption of several >100-Myr-old oceanic basins.

6.3.2. Subduction dynamics of the Halilbağı Complex

Within the Halilbağı Complex, the blueschist–eclogite domain and calc-schist–marble unit appear to have evolved separately (Çetinkaplan et al., 2008; Davis, 2011). Most of the mafic blocks in the blueschist–eclogite domain (e.g. HAL1255, HAL1243, HAL1241) were subjected to prograde metamorphism in the epidote stability field and subsequent pervasive re-equilibration often, but not always, in the lawsonite-blueschist facies. In contrast, mafic rocks in the calc-schist–marble unit (e.g. HAL1304) record essentially prograde metamorphism in the lawsonite stability field (Çetinkaplan et al. 2008; this study). Our garnet Lu–Hf dating results (Fig. 6) combined with the Lu distribution in garnet (Fig. 5) demonstrate that prograde metamorphism of HAL1304 (around 86 Ma) postdates peak to retrograde stages in the HAL1255 (92.4 Ma), HAL1243 (90.2 Ma) and HAL1241 (87.3 Ma). Assuming the lawsonite blueschist HAL1304 is representative of the calc-schist–marble unit, then the latter was subducted distinctly later than the rocks of the blueschist–eclogite domain. The sub-division of the Halilbağı Complex into two distinct tectonic formations therefore seems essential for our understanding of its tectonic evolution, with the blueschist–eclogite domain having formed during oceanic subduction, and the calc-schist–marble unit representing the leading edge of the Anatolide–Tauride continental margin (Fig. 9).

The epidote eclogite HAL1255, lawsonite–epidote blueschist HAL1243, and lawsonite–epidote interlayered blueschist and eclogite HAL1241 yielded distinct garnet Lu–Hf dates (Fig. 6), albeit weighted towards similar stages of garnet growth, i.e. between outer Grt_1 and inner Grt_2 (Fig. 5). Tectonic blocks within the blueschist–eclogite domain of the Halilbağı Complex that underwent different HP/LT metamorphic histories (Davis and Whitney, 2006; this study) therefore appear to have decoupled evolutions (Fig. 9). We note that prograde lawsonite, indicative of burial along a very low thermal gradient, is not restricted to the calc-schist–marble unit, as has been reported from the (northern) blueschist–eclogite domain (Davis and Whitney, 2006; this study). The array of P–T paths retrieved for different tectonic blocks (Davis and Whitney, 2006) and the distinct garnet Lu–Hf dates obtained for rocks with contrasting evolutions (this study) seem to preclude that the blueschist–eclogite domain constitutes a dismembered ophiolitic sequence—which would have a unique metamorphic evolution. We instead suggest that the blueschist–eclogite domain formed progressively over a few Myr through the accretion, at ~70–80 km depth, i.e. near the down-dip end

of slab–mantle decoupling (see Wada and Wang, 2009), of subducted oceanic sedimentary and mafic material, as previously proposed by Whitney et al. (2014).

Blueschist-facies retrogression in HAL1241 coeval with the prograde evolution of the lawsonite blueschist HAL1304 around 86 Ma (Fig. 9), as well as the widespread occurrence of pristine lawsonite, both prograde and retrograde, point to early exhumation in the active subduction channel. Lenses of HP/LT oceanic rocks thus appear to have been carried back along the plate interface as subduction progressed, so that the subduction channel may have been partitioned into a lower domain of descending material partly coupled to the down-going slab, and an upper domain of ascending material as theorised by England and Holland (1979), Shreve and Cloos (1986), and Gerya and Stöckhert (2002). Continuous return flow driven by buoyancy during on-going subduction (see (see Cloos, 1982; Gerya et al., 2002) was likely the main exhumation mechanism. Although no matrix (typically serpentinite or shale) seems to surround the HP/LT tectonic lenses (Fig. 1c), highly-strained, hydrated mafic and sedimentary rocks (now lawsonite blueschist) may have served as a low-viscosity, buoyant matrix, enabling mass return flow of hydrated, hence buoyant HP rocks. Such an interaction between mafic and sedimentary rocks at HP/LT conditions has been proposed by a recent oxygen-isotope study in the Halilbağı Complex (Gauthiez-Putallaz et al., 2014). Whether and how the blueschist–eclogite domain itself was compartmented and subjected to “continuous” return flow, previously envisaged by Whitney et al. (2014), remains a matter of ongoing research.

6.4. Thermal evolution of the subduction interface

The thermal evolution of juvenile subduction zones has been investigated numerically in several works (e.g., Hacker, 1990; Peacock, 1990; Kincaid and Sacks, 1997; Gerya et al., 2002), which demonstrated that the prograde P–T path followed by the top of the subducted crustal section gets significantly steeper (in P–T space) during the progressive refrigeration of the base of the overriding mantle wedge. However, the tempo of this evolution remains dependent on mechanical parameters and tectonic settings assumed by the models. Kincaid and Sacks (1997) tested various subduction rates (1.3–10 cm/yr) and suggested that a juvenile subduction interface attains thermal steady state after ~500–600 km of subduction, i.e. after only a few Myr for fast subduction, and over >30 Myr for slow subduction, whereas the slab age seems to play a secondary role. This result was in agreement

889 with the 10–15 Myr period inferred from the early models of Peacock (1990) set for an intermediate
890 subduction rate (3 cm/yr). In the model of Gerya et al. (2002), cooling of the slab interface
891 temperature at a depth of 100 km is substantial over at least 10 Myr after initiation, and continues, at
892 a lower rate, for another 15 Myr. Taking an upper-mantle perspective, Kelemen et al. (2003) reported
893 that thermal steady-state in the fore-arc mantle wedge is reached after ~10 Myr for any convergence
894 rate. In their obduction simulation, Duretz et al. (2016) observed that prograde P–T paths steepen
895 during at least 12 Myr after subduction initiation. In contrast to this general agreement between
896 models, Hall (2012) calculated that the slab interface at 60 km remains significantly above the
897 equilibrium temperature for tens of Myr.

898 Petrological and geochronological studies of subduction-related metamorphic rocks suggest
899 that cooling of a juvenile subduction interface is a long-lasting process. Anczkiewicz et al. (2004)
900 presented a range of five garnet Lu–Hf dates from 169 and 162 Ma for garnet amphibolite to 147 Ma
901 for glaucophane schist of the Franciscan Complex, California. The authors' interpretation that this
902 trend reflects the early cooling of the subduction zone was challenged by Page et al. (2007), who
903 argued that the regional-scale distribution of the studied samples allows the possibility that their
904 respective P–T evolutions are unrelated. The Rio San Juan Complex on Hispañola is another example
905 of subduction complex comprising a variety of metamorphic rocks. Krebs et al. (2008) presented
906 multi-method isotopic dates from three samples ranging from ~104 Ma (Lu–Hf in garnet) for an
907 eclogite that evolved along a counter-clockwise P–T path to 80–74 Ma (Rb–Sr and Ar–Ar in phengite)
908 for an omphacite blueschist, and 62 Ma (Rb–Sr in phengite) for a jadeite blueschist. Although the
909 assignment of phengite dates to certain P–T stages might not always be straightforward, the authors
910 argued for protracted cooling of the juvenile Lesser Antilles subduction zone.

911 In this study, we tested and validated the working hypothesis that the array of P–T paths
912 retrieved for various tectonic blocks within the Halilbağı Complex captures the progressive cooling of
913 the juvenile intra-Neotethys subduction zone. Garnet Lu–Hf geochronology applied to five samples of
914 mafic amphibolite, eclogite, and blueschist, combined with pseudosection modelling shed light on 15–
915 20-Myr of gradual steepening of prograde P–T path followed by the top of the subducting slab from
916 an oceanic-type geotherm of ~45 °C/km to a mature subduction-type thermal gradient of ~7 °C/km
917 (Fig. 9). We thus support conclusions reached by previous studies on other subduction complexes that

documented protracted thermal changes (e.g., Angiboust et al., 2016; Hyppolito et al., 2016), especially soon after subduction initiation (Anczkiewicz et al., 2004; Krebs et al., 2008).

The progression from the horizontal isotherms of an oceanic lithosphere to the strongly deflected thermal structure of a subduction zone involves thermal advection and dissipation (e.g., Peacock, 1990; Gerya et al., 2002; Kelemen et al., 2003; Hall, 2012). Crustal underplating at the bottom of the overriding mantle was also recently put forward as an effective mechanism to rapidly buffer the temperature in the upper part of the subduction channel, such that subducted rocks are subsequently dragged down against a colder upper plate, and thus metamorphosed along a colder HP path (see Agard and Vitale-Brovarone, 2013). Cooling of the subduction channel by underplating would be consistent with the metamorphism of the calc-schist–marble unit and possibly some of the underlying units (89–82 Ma phengite Ar–Ar dates; Seaton et al., 2014) along a lower thermal gradient than (the blocks of) the blueschist–eclogite domain. This scenario predicts that (i) the "cold" HP calc-schist–marble unit tectonically underlies the "warmer" blueschist–eclogite unit (so far, this configuration cannot be unequivocally established; see Fig. 1e,f); and (ii) "warmer" HP rocks (e.g. epidote eclogite) are concentrated along the contact with the overriding ophiolite, which detailed field work has precluded (Davis and Whitney, 2006; Whitney et al., 2014). Furthermore, cooling through underplating alone does not predict the occurrence of prograde lawsonite within the blueschist–eclogite unit (Davis and Whitney 2006; this study) and the close proximity in the field of tectonic blocks with contrasting P–T paths—unless invoking complete internal reorganisation of the complex. We therefore suggest that the subduction-channel cooling history inferred in this study (Fig. 9) involved mainly heat dissipation, which might explain its long duration.

7. Conclusions

In the present study, we tested the hypothesis that accretionary complexes comprising tectonic blocks with contrasting metamorphic P–T evolutions might record the thermal evolution of ancient subduction interfaces. Our petrochronological approach, based on petrography, mineral growth zoning, equilibrium phase diagrams, Lu distribution in garnet, and Lu–Hf geochronology, allowed deciphering and comparing the metamorphic evolution of individual HP oceanic blocks in the Halilbağı Complex (Anatolia). Our results reveal that HP/LT metamorphism in the mafic blocks of the Halilbağı

Complex was not synchronous but took place from ~92 to ~86 Ma with a progressively-decreasing thermal gradient. As indicated by the Lu–Hf garnet dates weighted toward the growth of post-peak rims, exhumation of HP tectonic blocks seems to have been continuous rather than episodic. "Warm" (i.e., prograde epidote–bearing) HP rocks appear to have formed earlier (~92 Ma) than "cold" (i.e., prograde lawsonite-bearing) ones (~87–86 Ma). In addition, the Lu–Hf garnet date and P–T estimates for the sub-ophiolitic metamorphic sole indicate that this intra-oceanic subduction zone initiated around 104 Ma near a mid-oceanic spreading centre, probably along a transform fault. At 86 Ma, when the leading edge of the continental margin was buried, the subduction interface was most likely thermally stable at ~7 °C/km. These results reveal 15–20 Myr of gradual cooling of a subduction interface following its formation. This time scale implies that the response of a subduction zone to changes in its thermal structure might be a relatively long-lasting process.

Acknowledgements

Funding by the Deutsche Forschungsgemeinschaft (project PO17-91) is kindly acknowledged. Warm thanks go to Roland Oberhänsli for supporting financially fieldwork in the study area. AP is especially grateful to Christine Fischer for her help with sample preparation, Franziska Scheffler and Roland Oberhänsli for assistance during fieldwork, and Chris Clark and Tim Johnson for sharing their expertise on LP/HT rocks. We thank Johann Diener for fruitful discussions and suggestions for pseudosection calculation, and Samuel Angiboust, Stephen Centrella, Ross Mitchell, and J. Brendan Murphy for insightful feedback during the preparation of this manuscript. Through comments by Philippe Agard and Alexis Plunder on an early version of the manuscript were highly appreciated. Constructive reviews by Besim Dragovic and an anonymous peer helped us to improve and clarify our manuscript.

References

Abers, G.A., Nakajima, J., van Keken, P.E., Kita, S., Hacker, B.R., 2013. Thermal–petrological controls on the location of earthquakes within subducting plates. Earth and Planetary Science Letters 369, 178-187.

Agard, P., Vitale-Brovarone, A., 2013. Thermal regime of continental subduction: The record from exhumed HP-LT terranes (New Caledonia, Oman, Corsica). Tectonophysics 601, 206-215.

977 Agard, P., Yamato, P., Jolivet, L., Burov, E., 2009. Exhumation of oceanic blueschists
978 and eclogites in subduction zones: timing and mechanisms. Earth Science Reviews
979 92, 53-79.
980 Agard, P., Yamato, P., Soret, M., Prigent, C., Guillot, S., Plunder, A., Dubacq, B.,
981 Chauvet, A., Monié, P., 2016. Plate interface rheological switches during subduction
982 infancy: Control on slab penetration and metamorphic sole formation. Earth and
983 Planetary Science Letters 451, 208-220.
984 Anczkiewicz, R., Platt, J.P., Thirlwall, M.F., Wakabayashi, J., 2004. Franciscan
985 subduction off to a slow start: evidence from high-precision Lu–Hf garnet ages on
986 high grade-blocks. Earth and Planetary Science Letters 225, 147–161.
987 Angiboust, S., Agard, P., Glodny, J., Omrani, J., Oncken, O., 2016. Zagros
988 blueschists: Episodic underplating and long-lived cooling of a subduction zone. Earth
989 and Planetary Science Letters 443, 48-58.
990 Angiboust, S., Agard, P., Jolivet, L., Beyssac, O., 2009. The Zermatt-Saas ophiolite:
991 the largest (60-km wide) and deepest (c. 70–80 km) continuous slice of oceanic
992 lithosphere detached from a subduction zone? Terra Nova 21, 171-180.
993 Aygül, M., Okay, A.I., Oberhänsli, R., Sudo, M., 2016. Pre-collisional accretionary
994 growth of the southern Laurasian active margin, Central Pontides, Turkey.
995 Tectonophysics 671, 218-234.
996 Bast, R., Scherer, E.E., Sprung, P., Fischer-Gödde, M., Stracke, A., Mezger, K., 2015.
997 A rapid and efficient ion-exchange chromatography for Lu-Hf, Sm-Nd, and Rb-Sr
998 geochronology and the routine isotope analysis of sub-ng amounts of Hf by MC-ICP-
999 MS. Journal of Analytical Atomic Spectrometry 30, 2323-2333.
1000 Baxter, E., Caddick, M., Dragovic, B., 2017. Garnet: A rock-forming mineral
1001 petrochronometer. Reviews in Mineralogy and Geochemistry 83, 469-533.
1002 Baxter, E.F., Scherer, E.E., 2013. Garnet geochronology: timekeeper of
1003 tectonometamorphic processes. Elements 9, 433-438.
1004 Bebout, G., 2007. Metamorphic chemical geodynamics of subduction zones. Earth
1005 and Planetary Science Letters 260, 373-393.
1006 Boudier, F., Ceuleneer, G., Nicolas, A., 1988. Shear zones, thrusts and related
1007 magmatism in the Oman ophiolite: initiation of thrusting on an oceanic ridge.
1008 Tectonophysics 151, 275-296.
1009 Boudier, F., Nicolas, A., 1985. Harzburgite and lherzolite subtypes in ophiolitic and
1010 oceanic environments. Earth and Planetary Science Letters 76, 84-92.
1011 Brown, M., 2002. Retrograde processes in migmatites and granulites revisited.
1012 Journal of Metamorphic Geology 20, 25-40.
1013 Candan, O., Çetinkaplan, M., Oberhänsli, R., Rimmelé, G., Akal, C., 2005. Alpine
1014 high-P/low-T metamorphism of the Afyon Zone and implications for the metamorphic
1015 evolution of Western Anatolia, Turkey. Lithos 84, 102.
1016 Çelik, O.F., Marzoli, A., Marschik, R., Chiaradia, M., Neubauer, F., Oz, I., 2011.
1017 Early-Middle Jurassic intra-oceanic subduction in the Izmir-Ankara-Erzincan Ocean,
1018 Northern Turkey. Tectonophysics 509, 120-134.
1019 Çetinkaplan, M., Candan, O., Oberhänsli, R., Bousquet, R., 2008. Pressure–
1020 temperature evolution of lawsonite eclogite in Sivrihisar; Tavşanlı Zone-Turkey.
1021 Lithos 104, 12-32.
1022 Çetinkaplan, M., Pourteau, A., Candan, O., Koralay, O.E., Oberhänsli, R., Okay, A.I.,
1023 Chen, F., Kozlu, H., Şengün, F., 2016. P–T–t evolution of eclogite/blueschist facies
1024 metamorphism in Alanya Massif: time and space relations with HP event in Bitlis
1025 Massif, Turkey. International Journal of Earth Sciences 105, 247-281.

1026 Clarke, S.M., Burley, S.D., Williams, G.D., Richards, A.J., Meredith, D.J., Egan, S.S.,
1027 2006. Integrated four-dimensional modelling of sedimentary basin architecture and
1028 hydrocarbon migration. Geological Society, London, Special Publications 253, 185-
1029 211.
1030 Cloos, M., 1982. Flow mélanges : Numerical modelling and geologic constraints on
1031 their origin in the Franciscan subduction complex, California. Bulletin of the
1032 Geological Society of America 93, 330-345.
1033 Daşçı, H.T., Parlak, O., Nurlu, N., Billor, Z., 2015. Geochemical characteristics and
1034 age of metamorphic sole rocks within a Neotethyan ophiolitic mélange from Konya
1035 region (central southern Turkey). Geodinamica Acta 27, 223-243.
1036 Davis, P.B., 2011. Petrotectonics of lawsonite eclogite exhumation: Insights from the
1037 Sivrihisar massif, Turkey. Tectonics 30.
1038 Davis, P.B., Whitney, D.L., 2006. Petrogenesis of lawsonite and epidote eclogite and
1039 blueschist, Sivrihisar Massif, Turkey. Journal of Metamorphic Geology 24, 823-849.
1040 Davis, P.B., Whitney, D.L., 2008. Petrogenesis and structural petrology of high-
1041 pressure metabasalt pods, Sivrihisar, Turkey. Contributions to Mineralogy and
1042 Petrology 156, 217-241.
1043 Dewey, J.F., Helman, M.L., Turco, E., Hutton, D.H.W., Knott, S.D., 1989.
1044 Kinematics of the Western Mediterranean, in: Coward, M.P., Dietrich, D., Park, R.G.
1045 (Eds.), Alpine Tectonics. Geological Society Special Publication, London, pp. 265-
1046 283.
1047 Diener, J., Powell, R., 2012. Revised activity–composition models for clinopyroxene
1048 and amphibole. Journal of Metamorphic Geology 30, 131-142.
1049 Dilek, Y., Thy, P., Hacker, B., Grundvig, S., 1999. Sructure and petrology of Tauride
1050 ophiolites and mafic dike intrusions (Turkey): implications for the Neotethyan ocean.
1051 Bulletin of the Geological Society of America 111, 1192-1216.
1052 Dilek, Y., Whitney, D.L., 1997. Counterclockwise P-T-t trajectory from the
1053 metamorphic sole a Neo-Thetyan ophiolite (Turkey). Tectonophysics 280, 295-310.
1054 Dragovic, B., Samanta, L.M., Baxter, E.F., Selverstone, J., 2012. Using garnet to
1055 constrain the duration and rate of water-releasing metamorphic reactions during
1056 subduction: an example from Sifnos, Greece. Chemical Geology 314, 9-22.
1057 Droop, G., 1987. A general equation for estimating Fe^{3+} concentrations in
1058 ferromagnesian silicates and oxides from microprobe analyses, using stoichiometric
1059 criteria. Mineralogical Magazine 51, 431-435.
1060 Duretz, T., Agard, P., Yamato, P., Ducassou, C., Burov, E.B., Gerya, T.V., 2016.
1061 Thermo-mechanical modeling of the obduction process based on the Oman ophiolite
1062 case. Gondwana Research 32, 1-10.
1063 Eberhart-Phillips, D., Reyners, M., 2001. A complex, young subduction zone imaged
1064 by three-dimensional seismic velocity, Fiordland, New Zealand. Geophysical Journal
1065 International 146, 731-746.
1066 El Korh, A., Schmidt, S.T., Ulianov, A., Potel, S., 2009. Trace element partitioning in
1067 HP–LT metamorphic assemblages during subduction-related metamorphism, Ile de
1068 Groix, France: a detailed LA-ICPMS study. Journal of Petrology 50, 1107-1148.
1069 England, P., Holland, T., 1979. Archimedes and the Tauern eclogites: the role of
1070 buoyancy in the preservation of exotic eclogite blocks. Earth and Planetary Science
1071 Letters 44, 287-294.
1072 Ernst, W., Liu, J., 1998. Experimental phase-equilibrium study of Al-and Ti-contents
1073 of calcic amphibole in MORB—a semiquantitative thermobarometer. American
1074 Mineralogist 83, 952-969.

1075 Ernst, W.G., 1988. Tectonic history of subduction zones inferred from retrograde
1076 blueschist p-t paths. Geology 16, 1081-1084.
1077 Federico, L., Crispini, L., Scambelluri, M., Capponi, G., 2007. Ophiolite mélange
1078 zone records exhumation in a fossil subduction channel. Geology 35, 499-502.
1079 Fornash, K.F., Cosca, M.A., Whitney, D.L., 2016. Tracking the timing of subduction
1080 and exhumation using 40. Contributions to Mineralogy and Petrology 171, 1-37.
1081 Galvez, M.E., Connolly, J.A., Manning, C.E., 2016. Implications for metal and
1082 volatile cycles from the pH of subduction zone fluids. Nature 539, 420-424.
1083 Gauthiez-Putallaz, L., Rubatto, D., Hermann, J., Martin, L., Fornash, K., Whitney, D.,
1084 2014. Sediment–eclogite fluid exchanges during subduction in the Tavşanlı zone,
1085 Turkey. Goldschmidt Abstracts 2014, 778.
1086 Gautier, Y., 1984. Deformations et métamorphisme associés à la suture téthysienne en
1087 Anatolie Centrale (Région de Sivrihisar, Turquie). Paris-Sud Orsay, p. 236.
1088 Gerya, T.V., Stöckhert, B., 2002. Exhumation rates of high pressure metamorphic
1089 rocks in subduction channels: The effect of Rheology. Geophysical Research Letters
1090 29, 1261.
1091 Gerya, T.V., Stöckhert, B., Perchuk, A., 2002. Exhumation of high-pressure
1092 metamorphic rocks in a subduction channel: A numerical simulation. Tectonics 21,
1093 1056.
1094 Göncüoglu, M.C., Sayit, K., Tekin, U.K., 2010. Oceanization of the northern
1095 Neotethys: geochemical evidence from ophiolitic melange basalts within the Izmir–
1096 Ankara suture belt, NW Turkey. Lithos 116, 175-187.
1097 Green, E., White, R., Diener, J., Powell, R., Holland, T., Palin, R., 2016. Activity–
1098 composition relations for the calculation of partial melting equilibria in metabasic
1099 rocks. Journal of Metamorphic Geology 34, 845-869.
1100 Grose, C.J., Afonso, J.C., 2013. Comprehensive plate models for the thermal
1101 evolution of oceanic lithosphere. Geochemistry, Geophysics, Geosystems 14, 3751-
1102 3778.
1103 Hacker, B.R., 1990. Simulation of the metamorphic and deformational history of the
1104 metamorphic sole of the Oman ophiolite. Journal of Geophysical Research 95, 4895-
1105 4907.
1106 Hacker, B.R., Mosenfelder, J.L., Gnos, E., 1996. Rapid emplacement of the Oman
1107 ophiolite: Thermal and geochronologic constraints. Tectonics 15, 1230-1247.
1108 Hacker, B.R., Peacock, S.M., Abers, G.A., Holloway, S.D., 2003. Subduction factory
1109 - 2. Are intermediate-depth earthquakes in subducting slabs linked to metamorphic
1110 dehydration reactions? Journal of Geophysical Research 108, 2030.
1111 Hall, P.S., 2012. On the thermal evolution of the mantle wedge at subduction zones.
1112 Physics of The Earth and Planetary Interiors 198–199, 9-27.
1113 Harris, N.B., Kelley, S., Okay, A.I., 1994. Post-collision magmatism and tectonics in
1114 northwest Anatolia. Contributions to Mineralogy and Petrology 117, 241-252.
1115 Harrison, T.M., 1982. Diffusion of 40Ar in hornblende. Contributions to Mineralogy
1116 and Petrology 78, 324-331.
1117 Holland, T., Powell, R., 2011. An improved and extended internally consistent
1118 thermodynamic dataset for phases of petrological interest, involving a new equation
1119 of state for solids. Journal of Metamorphic Geology 29, 333-383.
1120 Hyppolito, T., Angiboust, S., Juliani, C., Glodny, J., Garcia-Casco, A., Calderón, M.,
1121 Chopin, C., 2016. Eclogite-, amphibolite-and blueschist-facies rocks from Diego de
1122 Almagro Island (Patagonia): Episodic accretion and thermal evolution of the Chilean
1123 subduction interface during the Cretaceous. Lithos 264, 422-440.

Jochum, K.P., Nohl, U., Herwig, K., Lammel, E., Stoll, B., Hofmann, A.W., 2005. GeoReM: a new geochemical database for reference materials and isotopic standards. Geostandards and Geoanalytical Research 29, 333-338.

Kelemen, P.B., Rilling, J.L., Parmentier, E., Mehl, L., Hacker, B.R., 2003. Thermal structure due to solid‐state flow in the mantle wedge beneath arcs. Inside the subduction factory, 293-311.

Kelly, E., Carlson, W., Connelly, J., 2011. Implications of garnet resorption for the Lu–Hf garnet geochronometer: an example from the contact aureole of the Makhavinekh Lake Pluton, Labrador. Journal of Metamorphic Geology 29, 901-916.

Kincaid, C., Sacks, I.S., 1997. Thermal and dynamical evolution of the upper mantle in subduction zones. Journal of Geophysical Research 102, 12295-12315.

Kirby, S.H., 2000. Earth science: Taking the temperature of slabs. Nature 403, 31-34.

Kirby, S.H., Stein, S., Okal, E.A., Rubie, D.C., 1996. Metastable mantle phase transformations and deep earthquakes in subducting oceanic lithosphere. Reviews of Geophysics 34, 261-306.

Kohn, M.J., 2009. Models of garnet differential geochronology. Geochimica et Cosmochimica Acta 73, 170-182.

Krebs, M., Maresch, W., Schertl, H.-P., Münker, C., Baumann, A., Draper, G., Idleman, B., Trapp, E., 2008. The dynamics of intra-oceanic subduction zones: a direct comparison between fossil petrological evidence (Rio San Juan Complex, Dominican Republic) and numerical simulation. Lithos 103, 106-137.

Kriegsman, L.M., 2001. Partial melting, partial melt extraction and partial back reaction in anatectic migmatites. Lithos 56, 75-96.

Lagos, M., Scherer, E.E., Tomaschek, F., Münker, C., Keiter, M., Berndt, J., Ballhaus, C., 2007. High precision Lu-Hf geochronology of Eocene eclogite-facies rocks from Syros, Cyclades, Greece. Chemical Geology 243, 16-35.

Lapen, T.J., Johnson, C.M., Baumgartner, L.P., Mahlen, N.J., Beard, B.L., Amato, J.M., 2003. Burial rates during prograde metamorphism of an ultra-high-pressure terrane: an example from Lago di Cignana, western Alps, Italy. Earth and Planetary Science Letters 215, 57-72.

Locock, A.J., 2014. An Excel spreadsheet to classify chemical analyses of amphiboles following the IMA 2012 recommendations. Computers & Geosciences 62, 1-11.

Ludwig, K., 2012. Isoplot/Ex, v. 3.75. Berkeley Geochronology Center Special Publication 5.

Maffione, M., Thieulot, C., Van Hinsbergen, D.J., Morris, A., Plümper, O., Spakman, W., 2015. Dynamics of intraoceanic subduction initiation: 1. Oceanic detachment fault inversion and the formation of supra‐subduction zone ophiolites. Geochemistry, Geophysics, Geosystems 16, 1753-1770.

Meckel, T., Coffin, M., Mosher, S., Symonds, P., Bernardel, G., Mann, P., 2003. Underthrusting at the Hjort Trench, Australian-Pacific plate boundary: Incipient subduction? Geochemistry, Geophysics, Geosystems 4, 1099, doi:10.1029/2002GC000498.

Mehl, L., Hacker, B.R., Hirth, G., Kelemen, P.B., 2003. Arc-parallel flow within the mantle wedge: Evidence from the accreted Talkeetna arc, south central Alaska. Journal of Geophysical Research 108(B8), 2375.

Mulcahy, S., Vervoort, J., Renne, P., 2014. Dating subduction‐zone metamorphism with combined garnet and lawsonite Lu–Hf geochronology. Journal of Metamorphic Geology 32, 515-533.

Mulcahy, S.R., King, R.L., Vervoort, J.D., 2009. Lawsonite Lu-Hf geochronology: A new geochronometer for subduction zone processes. Geology 37, 987-990.

1174 Müller, R.D., Sdrolias, M., Gaina, C., Roest, W.R., 2008. Age, spreading rates, and
1175 spreading asymmetry of the world's ocean crust. Geochemistry, Geophysics,
1176 Geosystems 9, Q04006, doi:10.1029/2007GC001743.
1177 Müller, T., Dohmen, R., Becker, H., Ter Heege, J.H., Chakraborty, S., 2013. Fe–Mg
1178 interdiffusion rates in clinopyroxene: experimental data and implications for Fe–Mg
1179 exchange geothermometers. Contributions to Mineralogy and Petrology 166, 1563-
1180 1576.
1181 Münker, C., Weyer, S., Scherer, E., Mezger, K., 2001. Separation of high field
1182 strength elements (Nb, Ta, Zr, Hf) and Lu from rock samples for MC-ICPMS
1183 measurements. Geochemistry, Geophysics, Geosystems 2,
1184 https://doi.org/10.1029/2001GC000183.
1185 Nicolas, A., Boudier, F., Meshi, A., 1999. Slow spreading accretion and mantle
1186 denudation in the Mirdita ophiolite (Albania). Journal of Geophysical Research: Solid
1187 Earth 104, 15155-15167.
1188 Okay, A.I., 1986. High-pressure/low-temperature metamorphic rocks of Turkey.
1189 Geological Society of America Bulletin Memoir 164, 333–347.
1190 Okay, A.I., 2002. Jadeite–chloritoid–glaucophane–lawsonite blueschists in northwest
1191 Turkey: unusually high P/T ratios in continental crust. Journal of Metamorphic
1192 Geology 20, 757–768.
1193 Okay, A.I., Harris, N.B.W., Kelley, S.P., 1998. Exhumation of blueschists along a
1194 Tethyan suture in northwest Turkey. Tectonophysics 285, 275-299.
1195 Önen, A., Hall, R., 1993. Ophiolites and related metamorphic rocks from the Kütahya
1196 region, north‐west Turkey. Geological Journal 28, 399-412.
1197 Önen, A.P., 2003. Neotethyan ophiolitic rocks of the Anatolides of NW Turkey and
1198 comparison with Tauride ophiolites. Journal of the Geological Society 160, 947-962.
1199 Page, F.Z., Armstrong, L.S., Essene, E.J., Mukasa, S.B., 2007. Prograde and
1200 retrograde history of the Junction School eclogite, California, and an evaluation of
1201 garnet–phengite–clinopyroxene thermobarometry. Contributions to Mineralogy and
1202 Petrology 153, 533-555.
1203 Peacock, S.M., 1990. Numerical simulation of metamorphic pressure-temperature-
1204 time paths and fluid production in subducting slabs. Tectonics 9, 1197-1211.
1205 Peacock, S.M., 2009. Thermal and metamorphic environment of subduction zone
1206 episodic tremor and slip. Journal of Geophysical Research: Solid Earth 114.
1207 Peacock, S.M., van Keken, P.E., Holloway, S.D., Hacker, B.R., Abers, G.A.,
1208 Fergason, R.L., 2005. Thermal structure of the Costa Rica - Nicaragua subduction
1209 zone. Physics of The Earth and Planetary Interiors 149, 187.
1210 Peacock, S.M., Wang, K., 1999. Seismic Consequences of Warm Versus Coll
1211 Subduction Metamorphism: Examples from Southwest and Northeast Japan. Science
1212 286, 937-939.
1213 Peters, K., Smit, M., van Hinsbergen, D., van Roermund, H., Brouwer, F., 2017. The
1214 longevity of Neotethyan metamorphic soles from Lu-Hf garnet chronology, EGU
1215 General Assembly Conference Abstracts, p. 15673.
1216 Plunder, A., Agard, P., Chopin, C., Pourteau, A., Okay, A.I., 2015. Accretion,
1217 underplating and exhumation along a subduction interface: from subduction initiation
1218 to continental subduction (Tavşanlı zone, W. Turkey). Lithos 226, 233-254.
1219 Plunder, A., Agard, P., Chopin, C., Soret, M., Okay, A.I., Whitechurch, H., 2016.
1220 Metamorphic sole formation, emplacement and blueschist facies overprint: early
1221 subduction dynamics witnessed by western Turkey ophiolites. Terra Nova 28, 329-
1222 339.

Poli, S., Schmidt, M.W., 1995. H_2O transport and release in subduction zones: Experimental constraints on basaltic and andesitic systems. Journal of Geophysical Research 100, 22299-22314.

Pourteau, A., Bousquet, R., Vidal, O., Plunder, A., Duesterhoeft, E., Candan, O., Oberhänsli, R., 2014. Multistage growth of Fe–Mg–carpholite and Fe–Mg–chloritoid, from field evidence to thermodynamic modelling. Contributions to Mineralogy and Petrology 168, 1-25.

Pourteau, A., Candan, O., Oberhänsli, R., 2010. High-Pressure metasediments in central Turkey: Constraints on the Neotethyan closure history. Tectonics 29, TC5004, doi:10.1029/2009TC002650.

Pourteau, A., Oberhänsli, R., Candan, O., Barrier, E., Vrielynck, B., 2016. Neotethyan closure history of western Anatolia: a geodynamic discussion. International Journal of Earth Sciences 105, 203-224.

Pourteau, A., Sudo, M., Candan, O., Lanari, P., Vidal, O., Oberhänsli, R., 2013. Neotethys closure history of Anatolia: insight from ^{40}Ar–^{39}Ar geochronology and P–T estimation in high-pressure metasediments. Journal of Metamorphic Geology 31(6), 585-606.

Powell, R., Holland, T.J.B., 1988. An internally consistent thermodynamic dataset with uncertainties and correlations: 3. Applications to geobarometry, worked examples and a computer program. Journal of Metamorphic Geology 6, 173-204.

Rosenbaum, G., Lister, G.S., Duboz, C., 2002. Reconstruction of the tectonic evolution of the western Mediterranean since the Oligocene. Journal of the Virtual Explorer 8, 107-126.

Sarıfakıoğlu, E., Özen, H., Çolakoğlu, A., Sayak, H., 2010. Petrology, mineral chemistry, and tectonomagmatic evolution of Late Cretaceous suprasubduction - zone ophiolites in the İzmir–Ankara–Erzincan suture zone, Turkey. International Geology Review 52, 187-222.

Scherer, E., Münker, C., Mezger, K., 2001. Calibration of the lutetium-hafnium clock. Science 293, 683-687.

Scherer, E.E., Cameron, K.L., Blichert-Toft, J., 2000. Lu-Hf garnet geochronology: Closure temperature relative to the Sm-Nd system and the effects of trace mineral inclusions. Geochimica et Cosmochimica Acta 64, 3413-3432.

Schmidt, A., Pourteau, A., Candan, O., Oberhänsli, R., 2015. Lu–Hf geochronology on cm-sized garnets using microsampling: New constraints on garnet growth rates and duration of metamorphism during continental collision (Menderes Massif, Turkey). Earth and Planetary Science Letters 432, 24-35.

Schmidt, M.W., Poli, S., 1998. Experimentally based water budgets for dehydrating slabs and consequences for arc magma generation. Earth and Planetary Science Letters 163, 361-379.

Seaton, N.C., Teyssier, C., Whitney, D.L., Heizler, M.T., 2013. Quartz and calcite microfabric transitions in a pressure and temperature gradient, Sivrihisar, Turkey. Geodinamica Acta 26, 191-206.

Seaton, N.C.A., Whitney, D.L., Teyssier, C., Toraman, E., Heizler, M.T., 2009. Recrystallization of high-pressure marble (Sivrihisar, Turkey). Tectonophysics 479, 241-253.

Sengör, A.M.C., Yilmaz, Y., 1981. Tethyan Evolution of Turkey: A Plate Tectonic Approach. Tectonophysics 75, 181-241.

Sherlock, S., Kelley, S., Inger, S., Harris, N.B.W., Okay, A.I., 1999. 40Ar-39Ar and Rb-Sr geochronology of high-pressure metamorphism and exhumation history of the Tavşanlı Zone, NW Turkey. Contributions to Mineralogy and Petrology 137, 46-58.

1273 Sherlock, S.C., Arnaud, N.O., 1999. Flat plateau and impossible isochrons: Apparent
1274 40 Ar-39 Ar geochronology in a high-pressure terrain. Geochimica et Cosmochimica
1275 Acta 63, 2835-2838.
1276 Shin, T.A., Catlos, E.J., Jacob, L., Black, K., 2013. Relationships between very high
1277 pressure subduction complex assemblages and intrusive granitoids in the Tavşanlı
1278 Zone, Sivrihisar Massif, central Anatolia. Tectonophysics 595, 183-197.
1279 Shreve, R.L., Cloos, M., 1986. Dynamics of Sediment Subduction, Melange
1280 Formation, and Prism Accretion. Journal of Geophysical Research 91, 229-245.
1281 Skora, S., Baumgartner, L.P., Mahlen, N.J., Johnson, C.M., Pilet, S., Hellebrand, E.,
1282 2006. Diffusion-limited REE uptake by eclogite garnets and its consequences for Lu-
1283 Hf and Sm-Nd geochronology. Contributions to Mineralogy and Petrology 152, 703-
1284 720.
1285 Skora, S., Lapen, T.J., Baumgartner, L.P., Johnson, C.M., Hellebrand, E., Mahlen,
1286 N.J., 2009. The duration of prograde garnet crystallization in the UHP eclogites at
1287 Lago di Cignana, Italy. Earth and Planetary Science Letters 287, 402-411.
1288 Söderlund, U., Patchett, P.J., Vervoort, J.D., Isachsen, C.E., 2004. The 176 Lu decay
1289 constant determined by Lu–Hf and U–Pb isotope systematics of Precambrian mafic
1290 intrusions. Earth and Planetary Science Letters 219, 311-324.
1291 Soret, M., Agard, P., Dubacq, B., Plunder, A., Yamato, P., 2017. Petrological
1292 evidence for stepwise accretion of metamorphic soles during subduction infancy
1293 (Semail ophiolite, Oman and UAE). Journal of Metamorphic Geology 35(9), 1051-
1294 1080.
1295 Spandler, C., Hermann, J., Arculus, R., Mavrogenes, J., 2003. Redistribution of trace
1296 elements during prograde metamorphism from lawsonite blueschist to eclogite facies;
1297 implications for deep subduction-zone processes. Contributions to Mineralogy and
1298 Petrology 146, 205-222.
1299 Spandler, C., Pirard, C., 2013. Element recycling from subducting slabs to arc crust:
1300 A review. Lithos 170, 208-223.
1301 Speranza, F., Minelli, L., Pignatelli, A., Chiappini, M., 2012. The Ionian Sea: The
1302 oldest in situ ocean fragment of the world? Journal of Geophysical Research: Solid
1303 Earth 117, B12101, doi: 10.1029/2012JB009475.
1304 Spray, J.G., 1983. Lithosphere–asthenosphere decoupling at spreading centers and
1305 initiation of obduction. Nature 304, 253-255.
1306 Sprung, P., Scherer, E.E., Upadhyay, D., Leya, I., Mezger, K., 2010. Non-
1307 nucleosynthetic heterogeneity in non-radiogenic stable Hf isotopes: Implications for
1308 early solar system chronology. Earth and Planetary Science Letters 295, 1-11.
1309 Stampfli, G.M., Borel, G.D., 2002. A plate tectonic model for the Paleozoic and
1310 Mesozoic constrained by dynamic plate boundaries and restored synthetic oceanic
1311 isochrons. Earth and Planetary Science Letters 196, 17-33.
1312 Stern, R.J., Bloomer, S.H., 1992. Subduction zone infancy: examples from the Eocene
1313 Izu-Bonin-Mariana and Jurassic California arcs. Geological Society of America
1314 Bulletin 104, 1621-1636.
1315 Syracuse, E.M., van Keken, P.E., Abers, G.A., 2010. The global range of subduction
1316 zone thermal models. Physics of The Earth and Planetary Interiors 183, 73-90.
1317 Tian, Z., Wei, C., 2014. Coexistence of garnet blueschist and eclogite in South
1318 Tianshan, NW China: dependence of P‐T evolution and bulk‐rock composition.
1319 Journal of Metamorphic Geology 32, 743-764.
1320 Tribuzio, R., Messiga, B., Vannucci, R., Bottazzi, P., 1996. Rare earth element
1321 redistribution during high-pressure–low-temperature metamorphism in ophiolitic Fe-

gabbros (Liguria, northwestern Italy): Implications for light REE mobility in subduction zones. Geology 24, 711-714.
van Hinsbergen, D.J., Maffione, M., Plunder, A., Kaymakcı, N., Ganerød, M., Hendriks, B.W., Corfu, F., Gürer, D., Gelder, G.I., Peters, K., 2016. Tectonic evolution and paleogeography of the Kırşehir Block and the Central Anatolian Ophiolites, Turkey. Tectonics 35, 983-1014.
van Hinsbergen, D.J., Peters, K., Maffione, M., Spakman, W., Guilmette, C., Thieulot, C., Plümper, O., Gürer, D., Brouwer, F.M., Aldanmaz, E., 2015. Dynamics of intraoceanic subduction initiation: 2. Suprasubduction zone ophiolite formation and metamorphic sole exhumation in context of absolute plate motions. Geochemistry, Geophysics, Geosystems 16, 1771-1785.
van Keken, P.E., Hacker, B., Syracuse, E.M., Abers, G.A., 2011. Subduction factory: 4. Depth-dependent flux of H_2O from subducting slabs worldwide. Journal of Geophysical Research 116, B01401, doi: 10.1029/2010JB007922.
van Keken, P.E., Kiefer, B., Peacock, S.M., 2002. High-resolution models of subduction zones: Implications for mineral dehydration reactions and the transport of water into the deep mantle. Geochemistry, Geophysics, Geosystems 3, 1056, doi:10.1029/2001GC000256.
Vitale Brovarone, A., Beyssac, O., Malavieille, J., Molli, G., Beltrando, M., Compagnoni, R., 2013. Stacking and metamorphism of continuous segments of subducted lithosphere in a high-pressure wedge: The example of Alpine Corsica (France). Earth-Science Reviews 116, 35-56.
Wada, I., He, J., Hasegawa, A., Nakajima, J., 2015. Mantle wedge flow pattern and thermal structure in Northeast Japan: Effects of oblique subduction and 3-D slab geometry. Earth and Planetary Science Letters 426, 76-88.
Wada, I., Wang, K., 2009. Common depth of slab-mantle decoupling: Reconciling diversity and uniformity of subduction zones. Geochemistry, Geophysics, Geosystems 10, Q10009, doi:10.1029/2009GC002570.
White, R., Powell, R., Holland, T., Johnson, T., Green, E., 2014. New mineral activity–composition relations for thermodynamic calculations in metapelitic systems. Journal of Metamorphic Geology 32, 261-286.
Whitney, D.L., Davis, P.B., 2006. Why is lawsonite eclogite so rare? Metamorphism and preservation of lawsonite eclogite, Sivrihisar, Turkey. Geology 34, 473-476.
Whitney, D.L., Teyssier, C., Seaton, N.C., Fornash, K.F., 2014. Petrofabrics of high‐pressure rocks exhumed at the slab‐mantle interface from the "point of no return" in a subduction zone (Sivrihisar, Turkey). Tectonics 33, 2315-2341.
Whitney, D.L., Teyssier, C., Toraman, E., Seaton, N.C.A., Fayon, A.K., 2011. Metamorphic and tectonic evolution of a structurally continuous blueschist-to-Barrovian terrane, Sivrihisar Massif, Turkey. Journal of Metamorphic Geology 29, 193-212.
Woodcock, N., Robertson, A., 1977. Origins of some ophiolite-related metamorphic rocks of the "Tethyan" belt. Geology 5, 373-376.

Figure and table captions

Table 1 Modelled bulk-rock compositions for SIV1301 and HAL1304.

Table 2 Lu–Hf data.

Figure 1. Geology of the study area and sample locations. (a) Simplified tectonic map of the eastern Mediterranean showing the main Neotethyan sutures (with open triangles) and active subduction zones (with solid triangles). (b) Geological map of the central Sivrihisar Massif (modified after Davis and Whitney, 2006). (c) Detail of the Halilbağı Complex (modified after Çetinkaplan et al., 2008). (d, e) Alternative synthetic cross-sections, with P–T conditions as summarised by Davis (2011) and projected sample localities.

Figure 2. Photomicrographs of the investigated samples. (a) Upper amphibolite-facies assemblage Hbl–Pl–Grt–Di–Ilm in sample SIV1301 (PPL). Diopside is partially replaced by hornblende (white-filled arrows). Hornblende (Amp_2)–plagioclase (Pl_2)–albite symplectite (black-filled arrows) developed at the contact, especially between garnet and hornblende, possibly via 'reversal reaction' between a melt and its peritectic phases. Note that plagioclase grains occasionally host minute inclusions (amphibole and rare garnet) preferentially in their core. (b) Eclogitic assemblage Grt–Omp–Ep–Rt in lawsonite-free sample HAL1255 (cross-polarised light). (c) Euhedral garnet in textural equilibrium with the surrounding blueschist-facies matrix in sample HAL1243 (plane-polarised light, PPL). Note that garnet crystals are concentrated along a preferential layer. (d) Fragmented garnet porphyroblast displaying inclusion-rich interior and inclusion-poor outer rim in sample HAL1241. Lawsonite and omphacite are mainly present as crystal aggregates surrounded by a blueschist-facies matrix (PPL). (e) Back-scattered electron image of a garnet porphyroblast hosting a lawsonite inclusion in its core (see Fig. 2f). (f) Close-up of (e) showing the lack of Grt_2 fringe around the inclusions (including lawsonite), interpreted as prograde relicts. (g) Inclusion-rich garnet wrapped in a foliated blueschist-facies matrix in epidote-free sample HAL1304. Matrix foliation is marked by glaucophane, sodic clinopyroxene, and lawsonite (PPL). (h) Back-scattered electron image of an idiomorphic garnet crystal hosting pristine lawsonite inclusions. Titanite (barely distinct from garnet) occurs in garnet core, whereas rutile is observed in the rim. Mineral abbreviations are after Whitney and Evans (2010). The (i) denotes inclusions in garnet.

1397 **Figure 3.** Major-element zoning patterns of separated garnets from the studied samples. (a–e)
1398 Wavelength-dispersive X-ray fluorescence spectrometry maps of Mg (a) or Mn (b–e). (f–j) End-
1399 member proportions and Fe# (=Fe^{2+}/[Fe^{2+}+Mg]) values along rim–core–rim profiles.
1400
1401 **Figure 4.** Interpreted phase growth sequences in the studied samples reconstructed to account for
1402 textural observations and mineral growth zoning patterns.
1403
1404 **Figure 5.** Lutetium distribution in the investigated HP/LT garnet porphyroblasts. Left-hand panels
1405 show Lu concentration half-profiles. Right-hand panels show the distribution of the bulk-garnet Lu in
1406 concentric shells representing 10% volume steps from core to rim. Shaded regions behind the graphs
1407 indicate the locations of garnet growth zones defined mainly by Mn zoning and changes in inclusion
1408 assemblages (see Fig. 3b–e). Dashed vertical lines mark the 50:50 dividing line of the porphyroblast Lu
1409 budget.
1410
1411 **Figure 6.** Lutetium–hafnium isochron diagrams for the investigated samples. Two-point matrix– or
1412 wr–garnet isochron dates are given for each garnet aliquot and compiled in (f). Multi-point regression
1413 and two-point isochron dates in grey text (a–e) have apparently been affected by protracted garnet
1414 growth, disequilibrium growth, or incomplete spike–sample equilibration (see main text for details).
1415
1416 **Figure 7.** Pseudosections calculated for garnet amphibolite SIV1301 using a XRF-based bulk-rock
1417 composition and titration-determined Fe oxidation ratio $Fe^{3+}/\sum Fe$ = 0.23. (a) P–T diagram assuming
1418 excess H_2O. (b) T–M(H_2O) diagram at P = 0.6 GPa showing that the observed assemblage (in bold) is
1419 indicative of a H_2O-rich chemical system. Abbreviations of the modelled phases are given in the main
1420 text.
1421
1422 **Figure 8.** Pressure–temperature equilibrium phase diagrams for lawsonite blueschist HAL1304
1423 assuming excess H_2O and bulk-rock $Fe^{3+}/\sum Fe$ = 0.4. (a) Phase assemblage for a MnNCKFMASHTO bulk-
1424 rock composition (essentially the XRF analysis) prevailing during the formation of the garnet
1425 innermost core (prograde stage). (b) Phase assemblage for the NCKFMASHTO effective bulk

composition (corrected for the chemical fractionation of MnO in garnet) prevailing during the growth of the garnet outermost rim (peak stage). Abbreviations of the modelled phases are given in the main text.

Figure 9. (left) Hypothetical P–T–t evolution of the studied samples and progressive cooling of the subduction interface. (right) Tentative tectonic model evolution for the Halilbağı Complex, from subduction initiation at an oceanic transform fault around 104 Ma to incipient continental subduction at ca. 87 Ma.

Supplementary Material

Appendix A: XRF- and titration-based bulk-rock compositions of the investigated samples.

Appendix B: Representative mineral analyses of garnet, clinopyroxene, amphibole, and white mica.

Appendix C: LA-ICPMS trace-element profiles of garnets. Rim-to-rim profile for SIV1301; core-to-rim profiles for 'HAL' samples.

Appendix D: Details of the ion-exchange chromatography procedure.

Appendix E: Complementary information on the petrology of epidote eclogite HAL1255.

Table 1: Modelled bulk-rock compositions for SIV1301 and HAL1304

		SIV1301 garnet amphibolite Fig. 7a,b	**HAL 1304** lawsonite blueschist Fig. 8a	Fig. 8b
mol%	SiO2	47.46	53.74	54.85
	TiO2	0.47	0.95	1.01
	Al2O3	13.15	8.44	8.00
	FeO	11.28	9.86	8.59
	MnO	0.00	0.12	0.00
	MgO	9.78	13.20	13.97
	CaO	15.68	7.21	7.01
	Na2O	0.88	4.52	4.87
	K2O	0.02	0.01	0.01
	O	1.28	1.95	1.70

Table 2. Lu–Hf data.

sample and fraction	sieved size	Lu, ppm	Hf, ppm	$^{176}Lu/^{177}Hf$	est. 2 s.d. uncert. (%)	$^{176}Hf/^{177}Hf$	2 s.e. in 6th digit	est. 2 s.d. uncert. (%)
SIV1301—*garnet amphibolite*								
wr	powder	0.0290	0.0231	0.1780	0.44	0.284755	(18)	0.0092
Hbl-a	250–500 µm	0.0138	0.0468	0.04175	0.25	0.283447	(5)	0.0031
Hbl-b	250–500 µm	0.0164	0.0497	0.04691	0.43	0.283518	(13)	0.011
Grt-a	250–500 µm	0.510	0.00543	13.40	0.25	0.310855	(35)	0.019
Grt-b	125–250 µm	0.411	0.00612	9.573	0.25	0.302948	(29)	0.041
Grt-c	125–250 µm	0.437	0.00590	10.55	0.26	0.304811	(20)	0.015
HAL1255—*epidote eclogite*								
wr	powder	0.530	4.65	0.01618	0.25	0.282756	(4)	0.0028
mat	250–500 µm	0.212	0.284	0.1056	0.48	0.282963	(4)	0.0018
Grt-a	500–1000 µm	2.74	0.203	1.921	0.25	0.286079	(5)	0.0070
Grt-b	500–1000 µm	2.68	0.127	2.997	0.26	0.287949	(4)	0.0038
Grt-c	500–1000 µm	2.85	0.127	3.180	0.26	0.288279	(5)	0.0048
Grt-d	500–1000 µm	2.83	0.134	3.001	0.26	0.287969	(6)	0.0069
HAL1243—*lawsonite–epidote blueschist*								
wr	powder	0.790	3.08	0.03644	0.28	0.282958	(3)	0.0024
mat	125–250 µm	0.0945	0.108	0.1247	0.76	0.283189	(4)	0.0019
Grt-a	500–1000 µm	7.13	0.193	5.258	0.28	0.291828	(6)	0.0051
Grt-b	500–1000 µm	6.97	0.143	6.931	0.31	0.294716	(4)	0.0030
Grt-c	500–1000 µm	6.72	0.158	6.068	0.32	0.293175	(4)	0.0027
Grt-d	500–1000 µm	7.17	0.155	6.595	0.33	0.294086	(4)	0.0030
HAL1241—*lawsonite–epidote interlayered blueschist and eclogite*								
wr	powder	0.623	2.90	0.03048	0.27	0.283167	(3)	0.0024
mat	500–1000 µm	0.136	0.121	0.1593	0.38	0.283694	(7)	0.0055
Grt-a	500–1000 µm	2.23	0.139	2.280	0.26	0.287142	(5)	0.0050
Grt-b	500–1000 µm	2.26	0.118	2.729	0.26	0.287895	(4)	0.0030
Grt-c	500–1000 µm	2.32	0.119	2.760	0.27	0.288186	(4)	0.016
Grt-d	500–1000 µm	3.11	0.169	2.608	0.28	0.287681	(3)	0.0027
HAL1304—*lawsonite blueschist*								
wr	powder	0.326	1.87	0.02470	0.25	0.283200	(4)	0.0027
mat	250–500 µm	0.0690	0.0622	0.1575	0.25	0.283430	(6)	0.0046
Grt-a	500–1000 µm	3.70	0.0380	13.87	0.34	0.305592	(8)	0.0090
Grt-b	500–1000 µm	3.81	0.0540	10.04	0.55			
Grt-c	250–500 µm	3.91	0.0393	14.18	0.35	0.305974	(10)	0.0059
Grt-d	250–500 µm	3.22	0.0307	14.97	0.55	0.308065	(7)	0.0042
Grt-e	250–500 µm	3.56	0.0586	8.644	0.50			

wr = whole rock, Grt = garnet, mat = non-garnet and, to a certaint extent, non-lawsonite matrix minerals

Lower case letters in the name denote separate aliquots of a given batch of mineral separate grains.

Whole rocks were all fully digested in Teflon vials placed in high-pressure autoclaves (Parr bombs).

All other samples were digested on a hotplate in closed Teflon vials.

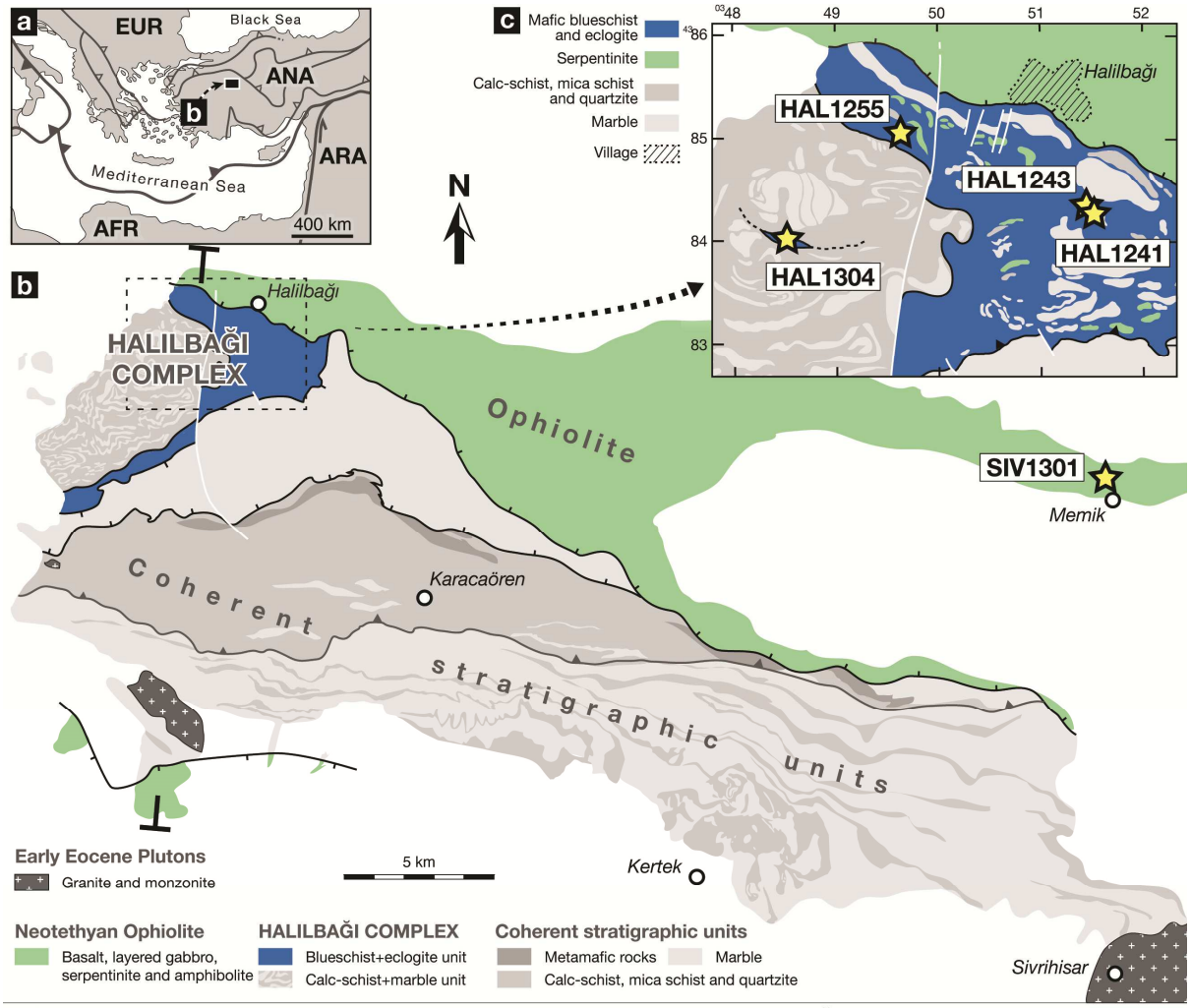
a
EUR
Black Sea
ANA
b
ARA
Mediterranean Sea
AFR
400 km
c
Mafic blueschist and eclogite
Serpentinite
Calc-schist, mica schist and quartzite
Marble
Village
N
03°48
49
50
51
52
43°86
85
84
83
Halilbağı
HAL1255
HAL1243
HAL1241
HAL1304
b
Halilbağı
HALILBAĞI COMPLEX
Ophiolite
SIV1301
Memik
Coherent stratigraphic units
Karacaören
Kertek
Sivrihisar
5 km
Early Eocene Plutons
Granite and monzonite
Neotethyan Ophiolite
Basalt, layered gabbro, serpentinite and amphibolite
HALILBAĞI COMPLEX
Blueschist+eclogite unit
Calc-schist+marble unit
Coherent stratigraphic units
Metamafic rocks
Marble
Calc-schist, mica schist and quartzite

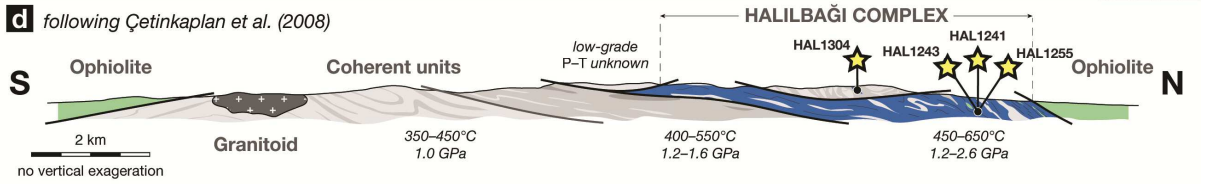
d
following Çetinkaplan et al. (2008)
HALILBAĞI COMPLEX
S
Ophiolite
Coherent units
low-grade
P–T unknown
HAL1304
HAL1243
HAL1241
HAL1255
Ophiolite
N
2 km
no vertical exageration
Granitoid
350–450°C
1.0 GPa
400–550°C
1.2–1.6 GPa
450–650°C
1.2–2.6 GPa

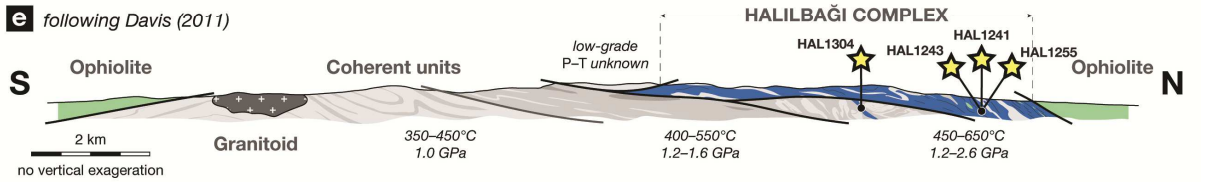
e
following Davis (2011)
HALILBAĞI COMPLEX
S
Ophiolite
Coherent units
low-grade
P–T unknown
HAL1304
HAL1243
HAL1241
HAL1255
Ophiolite
N
2 km
no vertical exageration
Granitoid
350–450°C
1.0 GPa
400–550°C
1.2–1.6 GPa
450–650°C
1.2–2.6 GPa

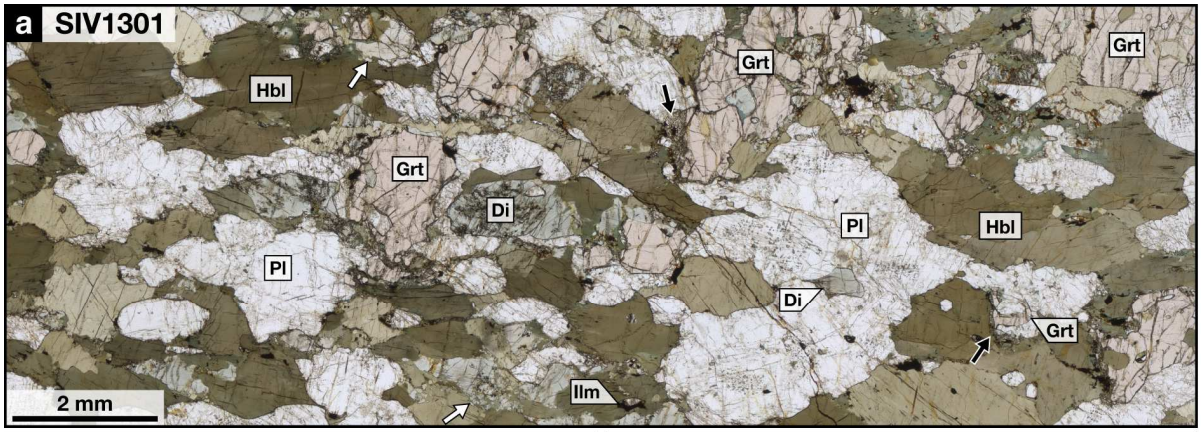
a SIV1301
Hbl
Grt
Grt
Grt
Di
Pl
Hbl
Pl
Di
Grt
Ilm
2 mm

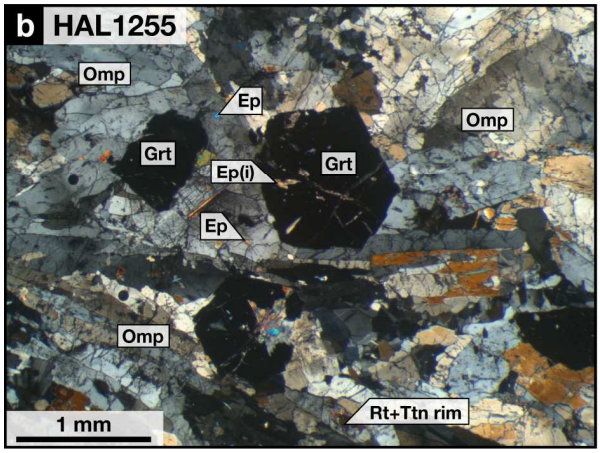
b HAL1255
Omp
Ep
Omp
Grt
Ep(i)
Grt
Ep
Omp
Rt+Ttn rim
1 mm

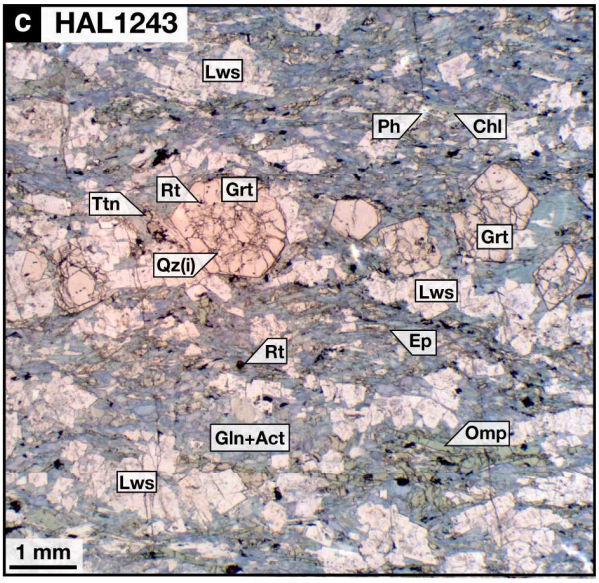
c HAL1243
Lws
Ph
Chl
Ttn
Rt
Grt
Grt
Qz(i)
Lws
Ep
Rt
Gln+Act
Omp
Lws
1 mm

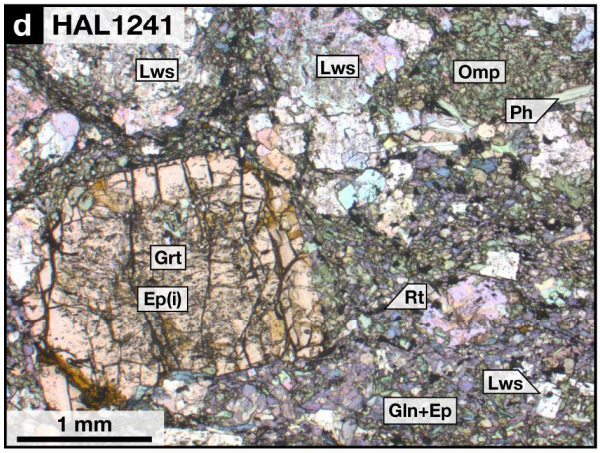
d HAL1241
Lws
Lws
Omp
Ph
Grt
Ep(i)
Rt
Lws
Gln+Ep
1 mm

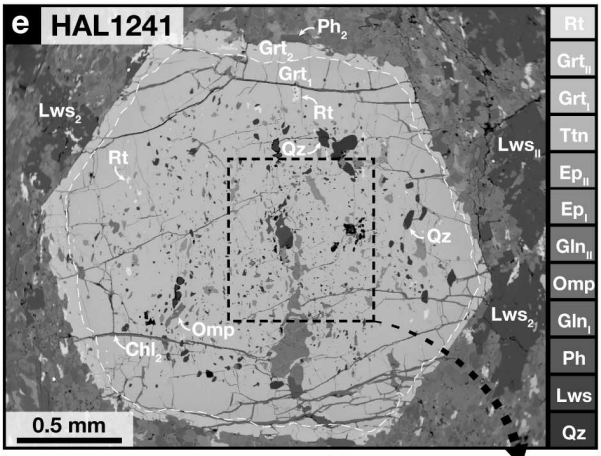
e HAL1241
Ph2
Grt2
Grt1
Lws2
Rt
Rt
Qz
Lws1
Qz
Omp
Chl2
Lws2
0.5 mm
Rt
Grt2
Grt1
Ttn
Ep2
Ep1
Gln2
Omp
Gln1
Ph
Lws
Qz

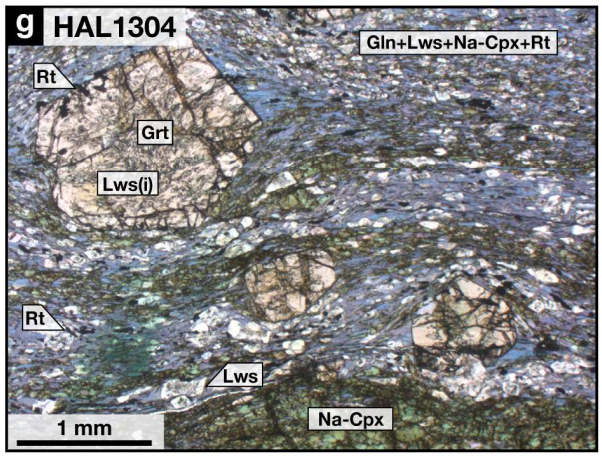
g HAL1304
Gln+Lws+Na-Cpx+Rt
Rt
Grt
Lws(i)
Rt
Lws
Na-Cpx
1 mm

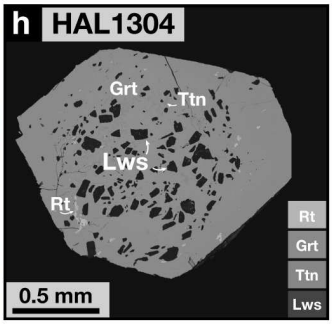
h HAL1304
Grt
Ttn
Lws
Rt
0.5 mm
Rt
Grt
Ttn
Lws

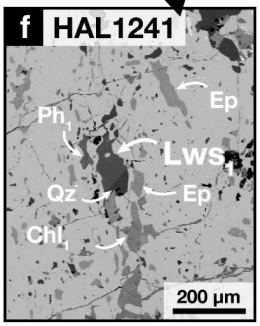
f HAL1241
Ep
Ph1
Lws1
Qz
Ep
Chl1
200 µm

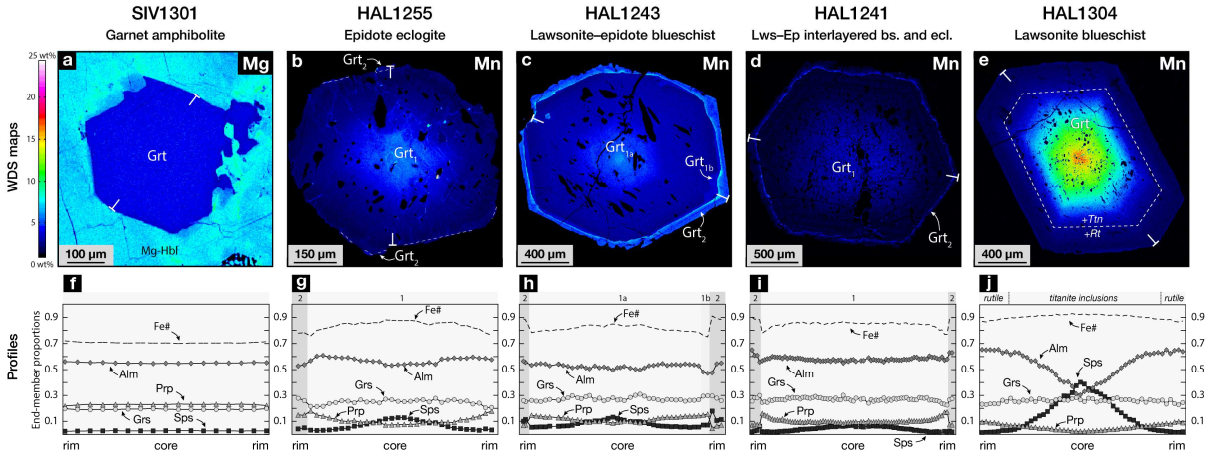

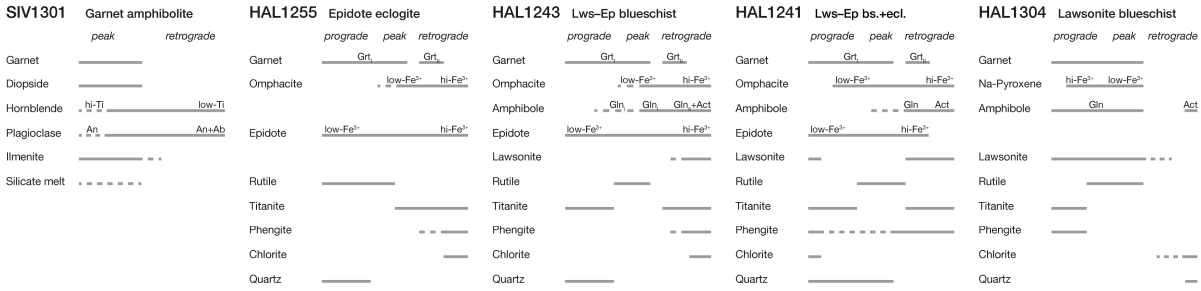

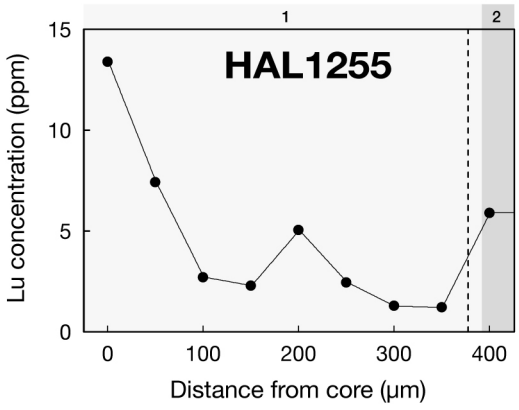
HAL1255
1
2
Lu concentration (ppm)
Distance from core (µm)

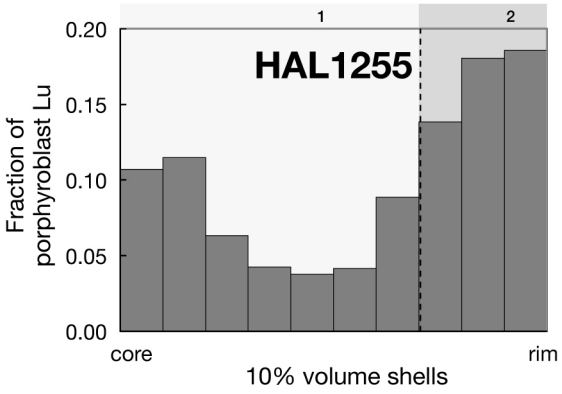
HAL1255
1
2
Fraction of porphyroblast Lu
core
rim
10% volume shells

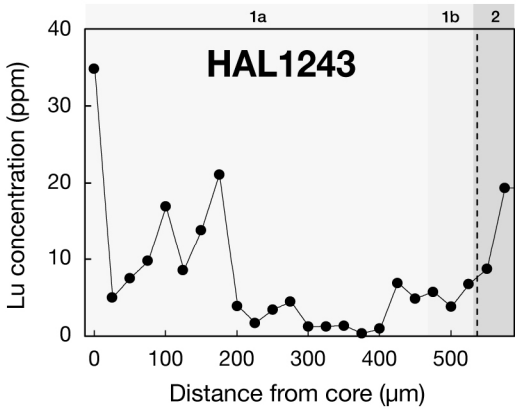
HAL1243
1a
1b
2
Lu concentration (ppm)
Distance from core (µm)

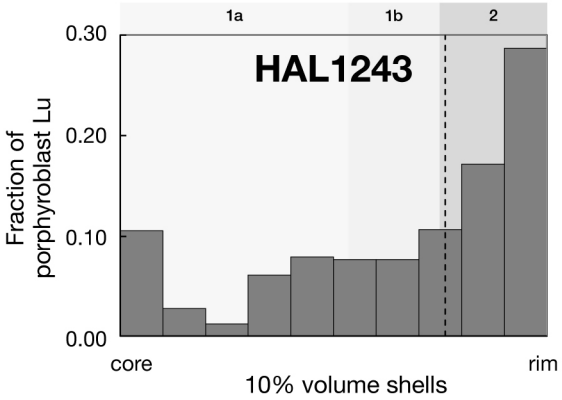
HAL1243
1a
1b
2
Fraction of porphyroblast Lu
core
rim
10% volume shells

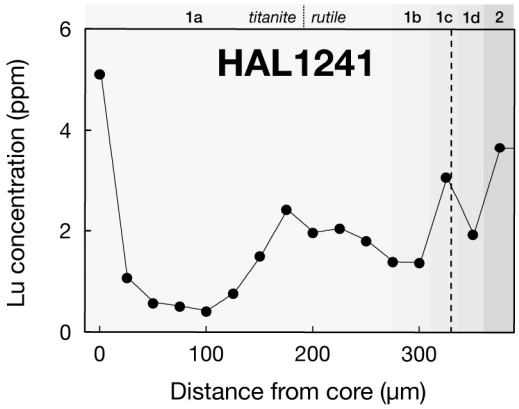
HAL1241
1a
titanite
rutile
1b
1c
1d
2
Lu concentration (ppm)
Distance from core (µm)

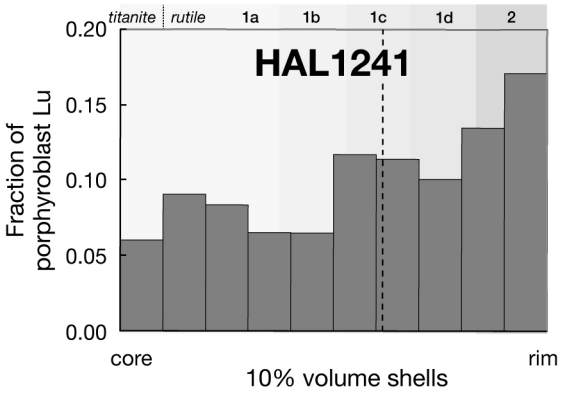
HAL1241
titanite
rutile
1a
1b
1c
1d
2
Fraction of porphyroblast Lu
core
rim
10% volume shells

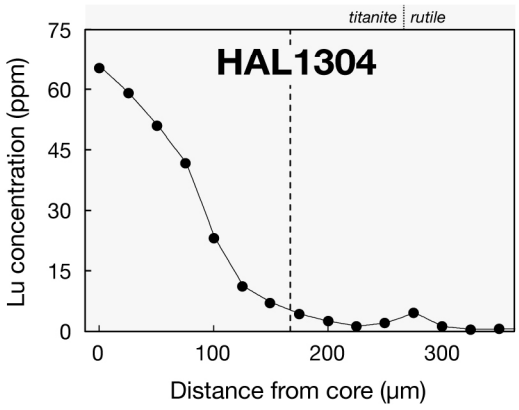
HAL1304
titanite
rutile
Lu concentration (ppm)
Distance from core (µm)

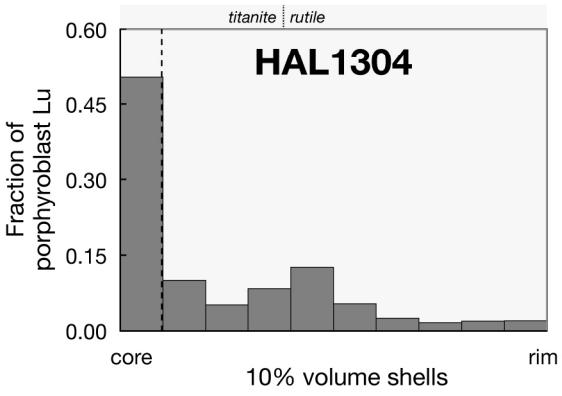
HAL1304
titanite
rutile
Fraction of porphyroblast Lu
core
rim
10% volume shells

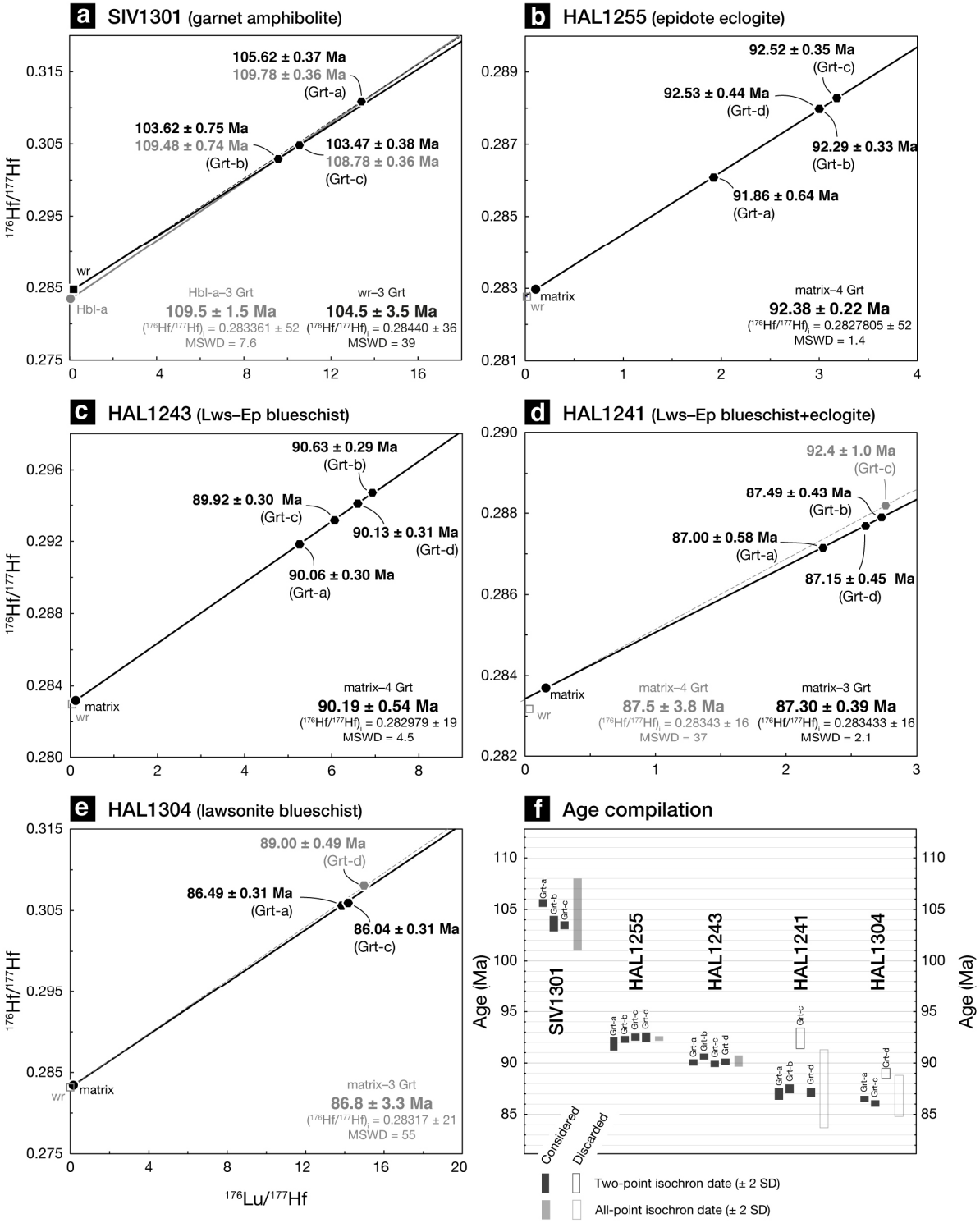
a SIV1301 (garnet amphibolite)
105.62 ± 0.37 Ma
109.78 ± 0.36 Ma
(Grt-a)
103.62 ± 0.75 Ma
109.48 ± 0.74 Ma
(Grt-b)
103.47 ± 0.38 Ma
108.78 ± 0.36 Ma
(Grt-c)
wr
Hbl-a
Hbl-a–3 Grt
109.5 ± 1.5 Ma
(176Hf/177Hf)i = 0.283361 ± 52
MSWD = 7.6
wr–3 Grt
104.5 ± 3.5 Ma
(176Hf/177Hf)i = 0.28440 ± 36
MSWD = 39
b HAL1255 (epidote eclogite)
92.52 ± 0.35 Ma
(Grt-c)
92.53 ± 0.44 Ma
(Grt-d)
92.29 ± 0.33 Ma
(Grt-b)
91.86 ± 0.64 Ma
(Grt-a)
matrix
wr
matrix–4 Grt
92.38 ± 0.22 Ma
(176Hf/177Hf)i = 0.2827805 ± 52
MSWD = 1.4
c HAL1243 (Lws–Ep blueschist)
90.63 ± 0.29 Ma
(Grt-b)
89.92 ± 0.30 Ma
(Grt-c)
90.13 ± 0.31 Ma
(Grt-d)
90.06 ± 0.30 Ma
(Grt-a)
matrix
wr
matrix–4 Grt
90.19 ± 0.54 Ma
(176Hf/177Hf)i = 0.282979 ± 19
MSWD = 4.5
d HAL1241 (Lws–Ep blueschist+eclogite)
92.4 ± 1.0 Ma
(Grt-c)
87.49 ± 0.43 Ma
(Grt-b)
87.00 ± 0.58 Ma
(Grt-a)
87.15 ± 0.45 Ma
(Grt-d)
matrix
wr
matrix–4 Grt
87.5 ± 3.8 Ma
(176Hf/177Hf)i = 0.28343 ± 16
MSWD = 37
matrix–3 Grt
87.30 ± 0.39 Ma
(176Hf/177Hf)i = 0.283433 ± 16
MSWD = 2.1
e HAL1304 (lawsonite blueschist)
89.00 ± 0.49 Ma
(Grt-d)
86.49 ± 0.31 Ma
(Grt-a)
86.04 ± 0.31 Ma
(Grt-c)
matrix
wr
matrix–3 Grt
86.8 ± 3.3 Ma
(176Hf/177Hf)i = 0.28317 ± 21
MSWD = 55
176Hf/177Hf
176Lu/177Hf
f Age compilation
Age (Ma)
SIV1301
HAL1255
HAL1243
HAL1241
HAL1304
Grt-a
Grt-b
Grt-c
Grt-d
Considered
Discarded
Two-point isochron date (± 2 SD)
All-point isochron date (± 2 SD)

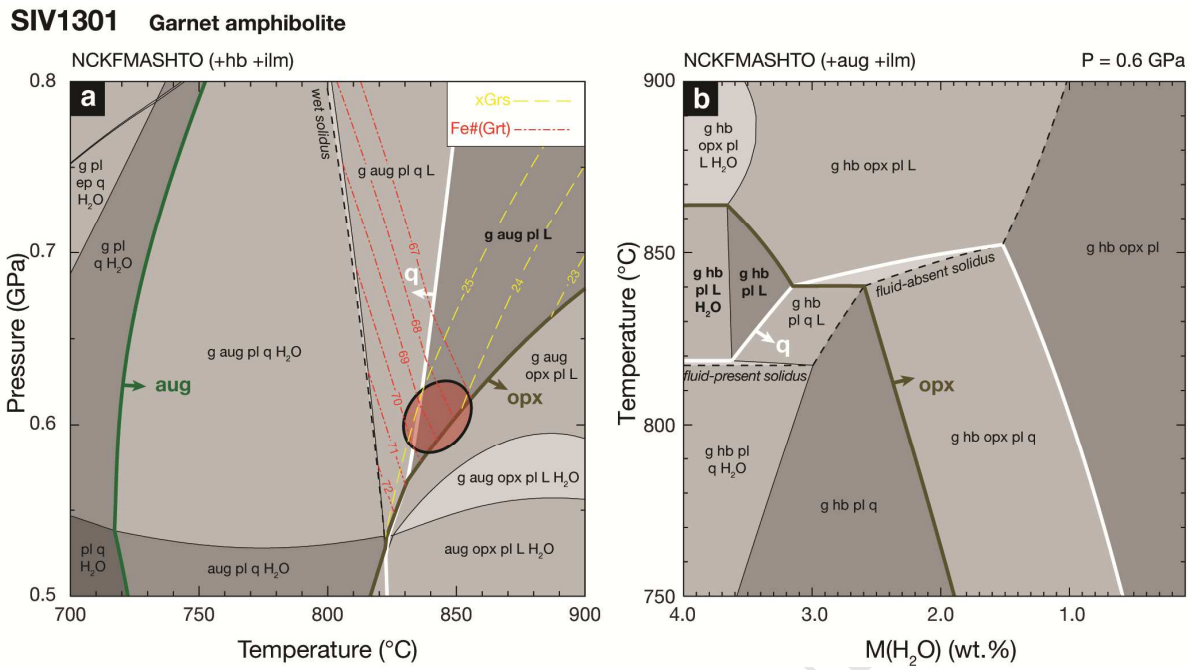

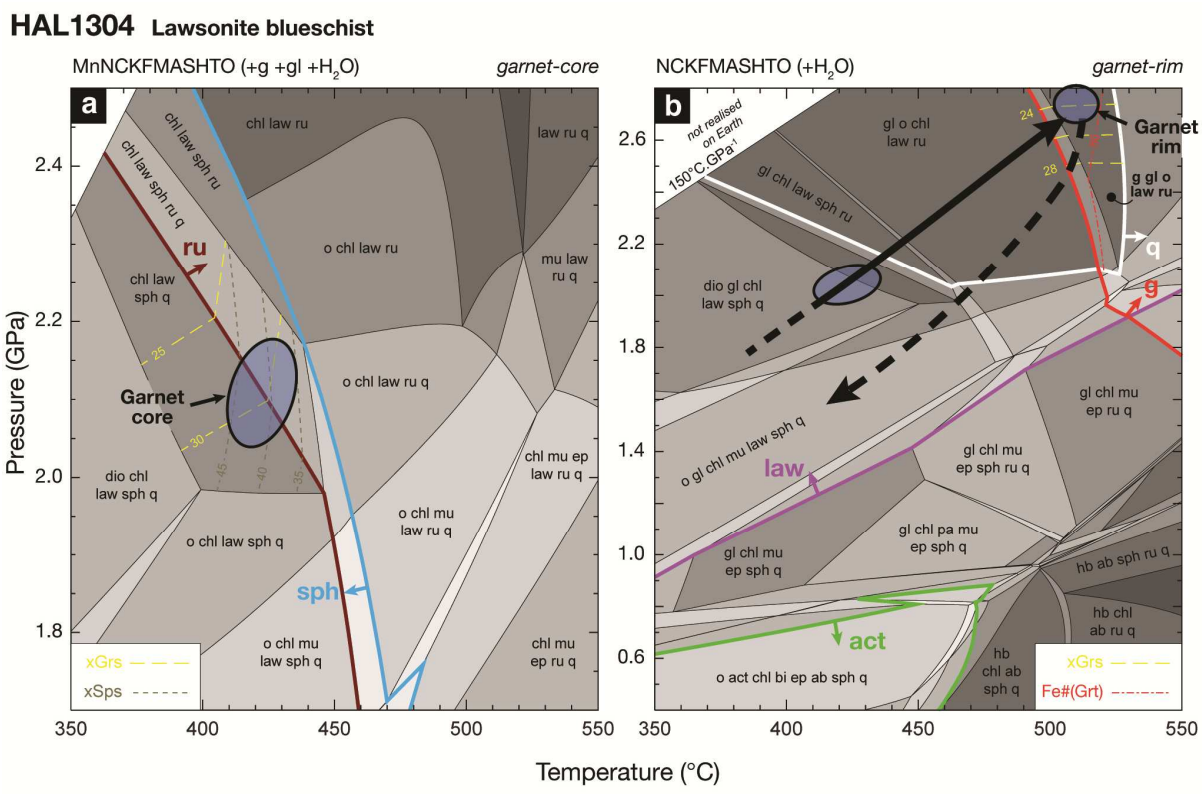

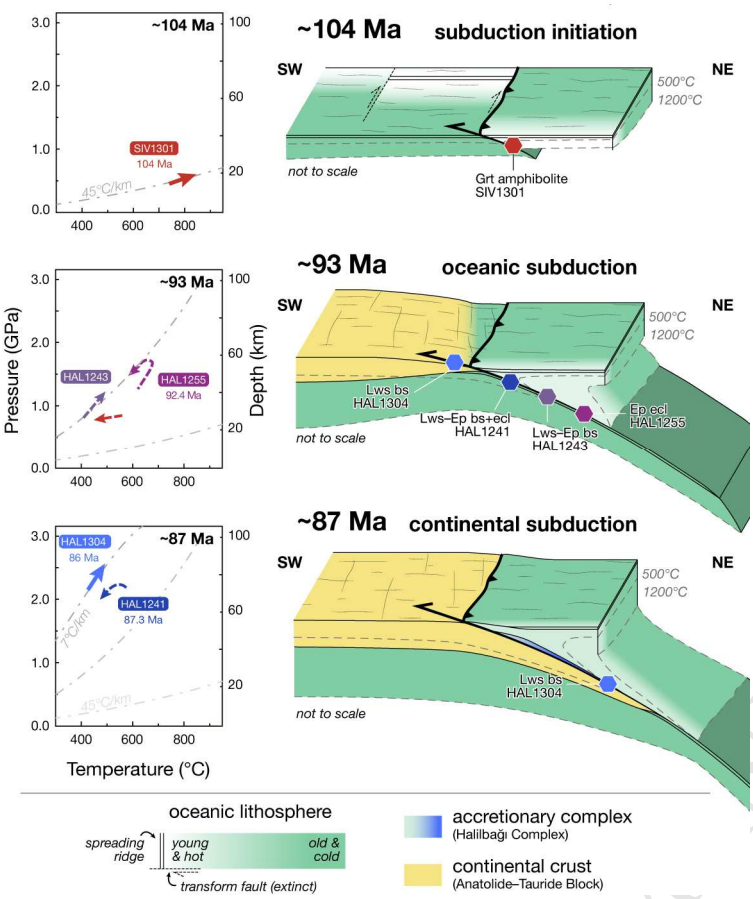

Thermal evolution of an ancient subduction interface revealed by Lu–Hf garnet geochronology, Halilbağı Complex (Anatolia)

Amaury Pourteau[a,d,*], Erik E. Scherer[b], Simon Schorn[c], Rebecca Bast[b,e], Alexander Schmidt[a], Lisa Ebert[a]

[a] *Institut für Erd- und Umweltwissenschaften, Universität Potsdam, Karl-Liebknecht-Straße 24–25, 14476 Potsdam–Golm, Germany*

[b] *Münster Isotope Research Centre, Institut für Mineralogie, Westfälische Wilhelms-Universität Münster, Corrensstraße 24, 48149 Münster, Germany*

[c] *Department of Geological Sciences, University of Cape Town, Private Bag X3, Rondebosch 7701, South Africa*

[d] *Earth Dynamics Research Group, ARC Centre of Excellence for Core to Crust Fluid Systems (CCFS), The Institute for Geoscience Research (TIGeR), School of Earth and Planetary Sciences, Curtin University, GPO Box U1987, WA 6845, Australia*

[e] *Institut für Geologie und Mineralogie, Universität zu Köln, Zülpicher Str. 49b, D-50674 Köln, Germany*

HIGHLIGHTS

- We constrain the oceanic subduction history of the Sivrihisar Massif
- Mafic amphibolite, eclogite and blueschist yield garnet Lu–Hf dates from 104 to 86 Ma
- Results reveal 15–20-Myr-long cooling of the ancient subduction interface
- Subduction started at a transform fault near a mid-oceanic spreading ridge